CANCER

Biomineralogical signatures of breast microcalcifications

Jennie A. M. R. Kunitake[1], Daniel Sudilovsky[2,3,4,5], Lynn M. Johnson[6], Hyun-Chae Loh[7], Siyoung Choi[8], Patrick G. Morris[9,10,11], Maxine S. Jochelson[12], Neil M. Iyengar[11,13], Monica Morrow[14], Admir Masic[7]*, Claudia Fischbach[8,15]*, Lara A. Estroff[1,15]*

Microcalcifications, primarily biogenic apatite, occur in cancerous and benign breast pathologies and are key mammographic indicators. Outside the clinic, numerous microcalcification compositional metrics (e.g., carbonate and metal content) are linked to malignancy, yet microcalcification formation is dependent on microenvironmental conditions, which are notoriously heterogeneous in breast cancer. We interrogate multiscale heterogeneity in 93 calcifications from 21 breast cancer patients using an omics-inspired approach: For each microcalcification, we define a "biomineralogical signature" combining metrics derived from Raman microscopy and energy-dispersive spectroscopy. We observe that (i) calcifications cluster into physiologically relevant groups reflecting tissue type and local malignancy; (ii) carbonate content exhibits substantial intratumor heterogeneity; (iii) trace metals including zinc, iron, and aluminum are enhanced in malignant-localized calcifications; and (iv) the lipid-to-protein ratio within calcifications is lower in patients with poor composite outcome, suggesting that there is potential clinical value in expanding research on calcification diagnostic metrics to include "mineral-entrapped" organic matrix.

INTRODUCTION

Pathological calcium mineral deposits, referred to as microcalcifications, are frequently associated with breast tumor development. Because of their x-ray opacity and potential association with malignancy, they are key clinical indicators assessed during mammographic breast cancer screening (1–4). Mammographic malignant calcifications lead to the identification of a reported one in five invasive breast cancers (5) and are crucial for detection of nonpalpable and small invasive breast cancers (6, 7). Only ~25% of biopsies based on suspicious calcification patterns, however, yield malignant pathologies; mammographic determination is complicated by the association of calcifications with numerous benign pathologies including sclerosing adenosis, duct ectasia, and fibroadenoma, among many others (3, 4). Malignant pathologies with associated calcifications include ductal carcinoma in situ (DCIS), where calcifications are mammographically detected in 72 to 97% of cases (2, 3), invasive ductal carcinoma [IDC; detected in ~18 to 54% of cases (3, 8, 9)],

and, less commonly, invasive lobular carcinoma [ILC; 1 to 24% (10)]. Calcifications are not considered prognostic markers, although an increasing body of clinical evidence suggests that specific subtypes of malignant calcifications are associated with more advanced disease and poorer patient prognosis including higher-grade cancers, increased risk of cancer recurrence, and higher mortality rates (2, 11). In addition, in vitro studies point to the possibility that mineral properties directly affect cancer cell behavior (12) and that more aggressive cancers may produce more calcifications (13). The contextual complexities surrounding both the diagnostic and prognostic potential of current calcification-based parameters, combined with the evidence that calcifications could directly contribute to or reflect tumor aggressiveness, provide a clear imperative to expand our analysis of these pathological biominerals to a resolution beyond their mammographic/histologic characteristics.

A framework for this analytical approach exists in the study of physiological biomineralization, e.g., the formation of bones and teeth in humans, which both informs our understanding of pathological mineralization and delineates the tools that can be harnessed to identify the key features of the associated organic-inorganic environment (14). High-resolution materials characterization has shown that organic matrix components are intimately associated with physiological biominerals and are mechanistically and physically integral to the mineralization process as templates, regulators, compartments, and/or shuttles of mineral precursors (15–17). Furthermore, micrometer-scale mapping of biominerals has revealed spatial variations in mineral and matrix composition with functional and mechanistic implications (18–20). Similar characterization techniques, applied to pathological calcifications, have unearthed clues into the dysregulated processes involved in the formation of retinal drusen (21), cardiovascular calcifications (22), and dental plaque (23). Mineral characterization techniques can even provide a diagnostic basis for disease etiology, as in kidney stones (24, 25), and clinical integration of many of these techniques is underway or

[1]Department of Materials Science and Engineering, Cornell University, Ithaca, NY 14850, USA. [2]Department of Pathology and Laboratory Medicine, Cayuga Medical Center at Ithaca, Ithaca, NY 14850, USA. [3]Pathology Department, Kingman Regional Medical Center, Kingman, AZ 86409, USA. [4]Pathology Department, Western Arizona Medical Center, Bullhead City, AZ 86442, USA. [5]Pathology Department, Yuma Regional Medical Center, Yuma, AZ 85364, USA. [6]Cornell Statistical Consulting Unit, Cornell University, Ithaca, NY 14850, USA. [7]Department of Civil and Environmental Engineering, Massachusetts Institute of Technology, Cambridge, MA 02139, USA. [8]Nancy E. and Peter C. Meinig School of Biomedical Engineering, Cornell University, Ithaca, NY 14850, USA. [9]Medical Oncology Service, Beaumont Hospital, Dublin, Ireland. [10]Breast Medicine Service, Department of Medicine, Memorial Sloan Kettering Cancer Center/Evelyn H. Lauder Breast and Imaging Center, New York, NY 10065, USA. [11]Department of Medicine, Weill Cornell Medical College, New York, NY 10021, USA. [12]Department of Radiology, Memorial Sloan Kettering Cancer Center/Evelyn H. Lauder Breast and Imaging Center, New York, NY 10065, USA. [13]Department of Medicine, Memorial Sloan Kettering Cancer Center, New York, NY 10065, USA. [14]Breast Service, Department of Surgery, Memorial Sloan Kettering Cancer Center, New York, NY 10065, USA. [15]Kavli Institute at Cornell for Nanoscale Science, Cornell University, Ithaca, NY 14850, USA.
*Corresponding author. Email: lae37@cornell.edu (L.A.E.); cf99@cornell.edu (C.F.); masic@mit.edu (A.M.)

proposed (26). Thus, using techniques capable of quantifying the composition of breast microcalcifications could offer a biomineralization-based analytical axis for breast cancer diagnosis and prognosis, e.g., can specific inorganic or "entrapped" organic moieties serve as chemical indicators of cancer aggressiveness?

A mounting body of evidence points in this direction, suggesting that, beyond the mammogram, the biomineralogical composition of microcalcifications holds promise for both diagnosis (i.e., defining the nature of the pathology) or even prognosis (i.e., predicting the course of the disease). Numerous reports of mineral compositional metrics with links to malignancy have been reported. Although mineral phase can vary [for a recent review, see (14)], the most frequently encountered, and the focus of this work, is carbonated bioapatite (which we refer to as "apatite"). This form of apatite is structurally based on geologic hydroxy(l)apatite [$Ca_{10}(PO_4)_6OH_2$] (14, 27–29), bearing numerous substitutions, many of which have been implicated in malignancy, including carbonate and metal ions (30), and associated organic matrix. Note that although the mineral component of breast calcifications bears resemblance to bone apatite, osseous metaplasia (the presence of bone tissue and/or heterotopic ossification) of the breast is rare (4) and, with the exception of some benign fibroadenomas (14, 31), intrafibrillar mineralization of collagen in breast tissue is rarely encountered. In microcalcifications, relative carbonate content has been shown to be reduced for those found in malignant versus benign regions (27, 29, 32). Decreased crystallinity (size and perfection), enhanced sodium (33), localized metal ions (28, 34, 35), and alterations in organic matrix content (28, 29, 31, 36) have also been reported for calcifications in malignant versus benign tissue. Magnesium and microcalcifications composed of the magnesium-bearing calcium phosphate phase, whitlockite [$Ca_{18}(Mg)_2(HPO_4)_2(PO_4)_{12}$] (37), have received attention, but association with malignancy is debated (29, 33, 38, 39). Although potentially the most direct line to cancer and host biology, less is known about the organic matrix: Classes of biomolecules have been identified within calcifications (28, 40), and the organic matrix-to-mineral ratio was shown to be relatively increased in malignant calcifications, particularly in DCIS (27, 29).

Promising compositional metrics have emerged from individual and bulk analyses of microcalcifications, yet few studies have mapped the spatial heterogeneity of these metrics across pathologies within intact tissue samples. Understanding the extent of both pathological and spatial heterogeneity of microcalcification composition (4, 14) is crucial to assessing the diagnostic/prognostic value of these metrics as well as developing predictive models that could incorporate "biomineralogical signatures." Furthermore, although microcalcifications present frequently in DCIS, the prognostic value of their compositional metrics remains unclear. In this work, we map calcifications from human breast tissue samples (Fig. 1) within their chemically distinctive surrounding organic matrices at submicrometer resolution across a range of pathologies. The objective of this exploratory study is to investigate the association of calcification mineral properties, e.g., the biomineralogical signatures, and pathological parameters, both at the local (i.e., the tissue surrounding the calcification) and patient level (i.e., the overall patient diagnosis). We use Raman microscopy, a powerful, nondestructive technique (19, 22, 23, 28, 41) based on a clinically relevant spectroscopy (42, 43), and show the value of Raman to augment conventional histopathological evaluation. To interrogate the

effects of physiochemical heterogeneity on calcification composition, we take an omics-inspired approach (44): For 93 calcifications across 21 patients, we acquire spatially registered Raman microscopy and energy-dispersive spectroscopy (EDS) mapping measurements (28) and collectively define a biomineralogical signature for each calcification, together with serial histopathology used to classify the surrounding pathology and tissue environment (Fig. 2).

RESULTS
Calcifications across diverse pathologies and environments are primarily apatite with a colocalized organic matrix

To investigate the association of calcification mineral properties and pathological parameters, frozen breast tumor tissue samples, banked at Memorial Sloan Kettering Cancer Center, in which mineral presence was observed upon histological evaluation at the time of patient diagnosis, were randomly selected (40 in total) and serially cryosectioned (Fig. 1). Two of these sections underwent histological staining for identification of calcium phosphate regions of interest (von Kossa) and for classification of pathology corresponding to calcification regions [hematoxylin and eosin (H&E)]. On the basis of staining and subsequent Raman analysis, calcifications were detected in a total of 21 of 40 sectioned patient samples (Fig. 1). Patient diagnoses were primarily invasive breast cancer (19 ductal and 1 lobular) with one instance of DCIS (1 of 21). However, an invasive component was not always present on sectioning or lacked apparent calcifications. The calcification population therefore includes, in addition to invasive pathologies, DCIS and cancer-entrapped or cancer-adjacent benign regions (Fig. 1). Calcification regions within the final, unstained, serial section were analyzed using both Raman microscopy and EDS to define the biomineralogical signature (Fig. 2). To preserve tissue structure and to maintain more physiological conditions, tissue specimens were immersed in buffer during Raman measurements. Raman maps were acquired for a total of 117 calcification regions, nine of which were included in earlier studies (14, 28). Calcifications ranged in cross-sectional size from <1 μm² to 0.4 mm². The patient data and biomineralogical signature measurements can be found in data file S1.

Most mineral spectra within Raman maps are consistent with B-type carbonated apatite, where carbonate ions substitute a fraction of phosphate ions (30), with a ν_1 phosphate band situated at ~962 cm⁻¹, the ν_1 B-type carbonate band evident at ~1075 cm⁻¹, and peak envelope shapes and positions consistent with the bands emergent from the phosphate ν_2 (~430 cm⁻¹) and ν_4 (~580 cm⁻¹) vibrational modes (45). Apatite inverse basis spectra, where the organic matrix has been subtracted from the mineral spectra semi-automatically (Fig. 2), showed multiple weak bands or shoulders attributable to acid phosphate (HPO_4^{2-}), including ~550, ~878 to 923, and 1004 cm⁻¹ (23, 46–48), particularly in calcifications containing low carbonate (fig. S1). No clear evidence of A-type carbonate substitution, substitution at a hydroxyl site rather than a phosphate site (30), was detected. Secondary electron (SE) and backscatted electron (BSE) images showed that apatite manifested as multiple morphologies including spheroidal, compact, and laminate (figs. S2 to S4). Laminate structures, reminiscent of other pathological minerals (14, 49–51), have been previously described in microcalcifications (14, 52), and their presence may indicate a periodic or intermittent deposition process. Whitlockite-like mineral was found, although only
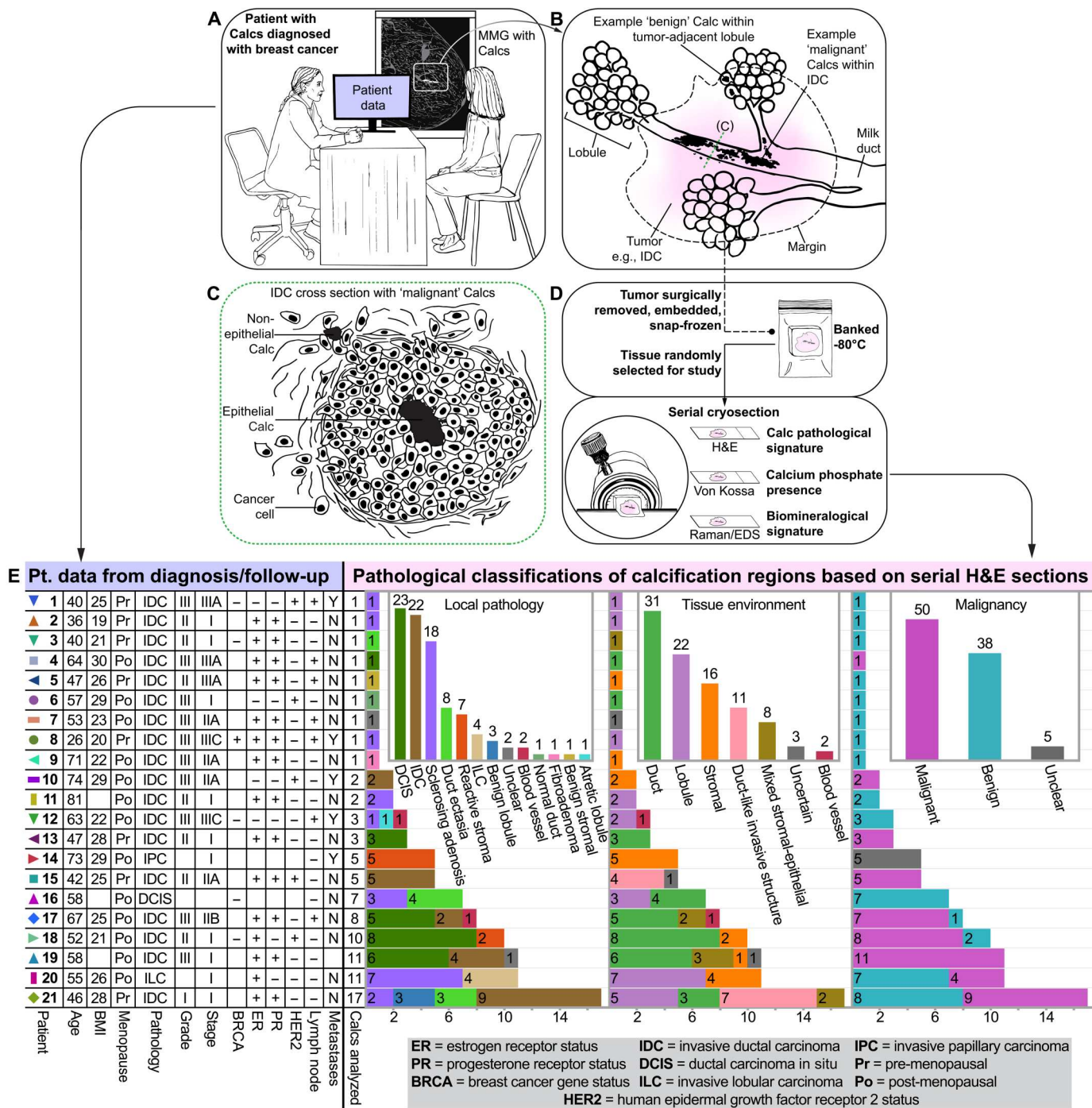
Fig. 1. Breast cancer patient sample flow (with anatomical context) and table of breast cancer patient data and pathology of calcification regions. (**A**) Schematic depicting an example patient diagnosed with breast cancer, with calcifications (Calcs) present on the mammogram (MMG). Patient data collected at diagnosis are stored and later deidentified if the patient is selected for the study. (**B**) Schematic magnification of the calcification region from the mammogram in (A) showing a milk duct and lobule with a region of IDC (pink) and associated malignant mineral. Surgical excision of the tumor (dashed line) also extracts an example tumor-adjacent calcification situated in a benign lobule. (**C**) Schematic cross-section of the duct from (B) showing IDC. Cancer cells are both within and invading outside the duct into the surrounding connective tissue (stroma). Example malignant epithelial and nonepithelial calcifications are indicated. (**D**) Scheme showing that, upon surgical removal of the tumor (via lumpectomy or mastectomy), a portion was embedded, snap-frozen, and banked at −80°C. After selection for this study, tissue was serially cryosectioned for pathological and biomineralogical analysis. Note that the schematic is not to scale. (**E**) Table of patient and calcification data. Patient data collected at diagnosis and follow-up data (metastases) are shown (left; purple). For each patient, the number of analyzed calcification regions within sectioned tissue [as shown in (D)] is given and broken down by pathological classifications (right, pink) determined from the serial H&E section. Combined totals across patients for these classifications are shown in insets. Pathological classification is described in Supplementary Text (page 2, "Calcification classifications" section). Patient-specific symbols/markers and numbers are shown (left) and used throughout the study.
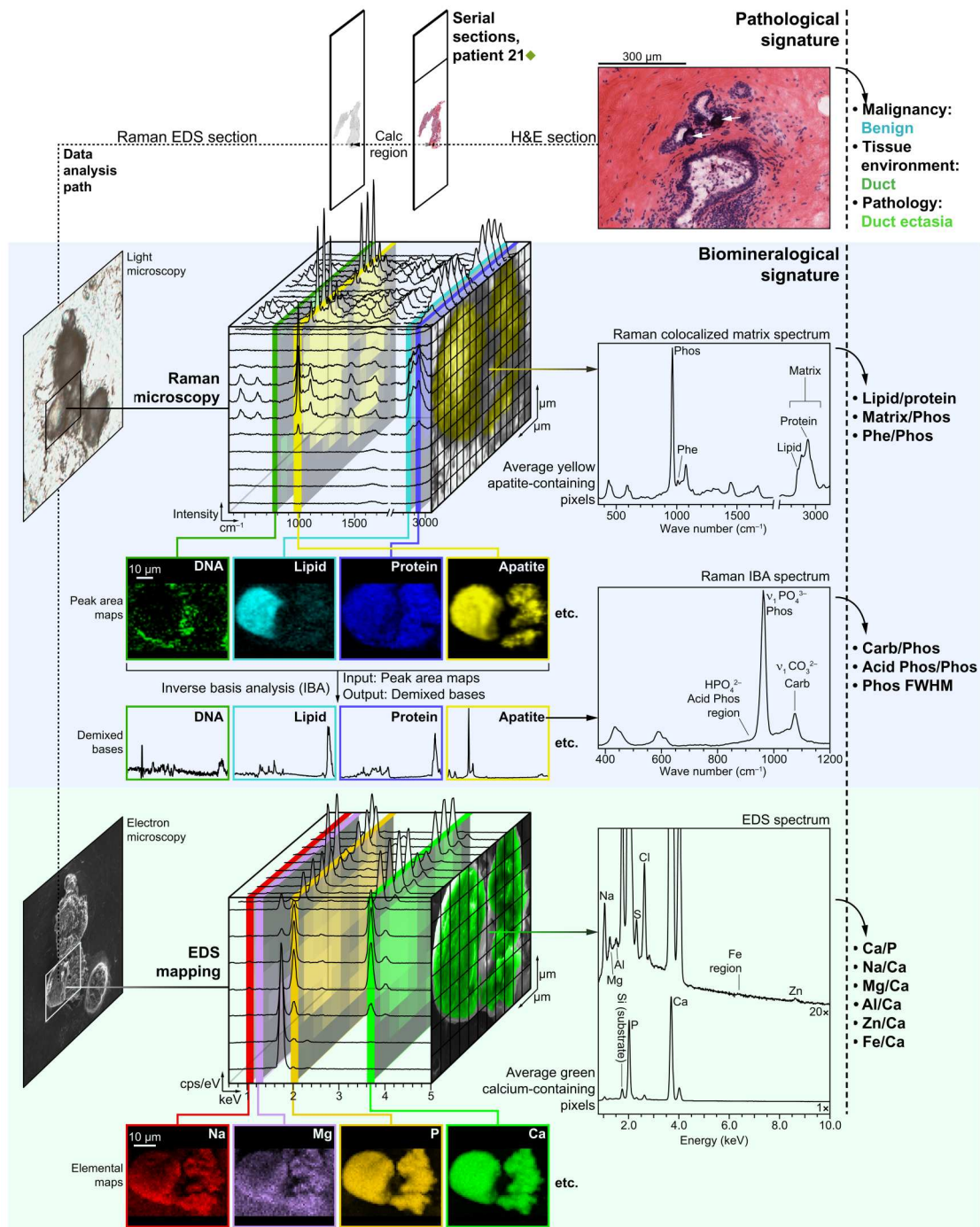
Fig. 2. Schematic depicting data analysis flow. The schematic shows how the pathological and biomineralogical signatures are generated for a sample benign (micro)-calcification (Calc) region within sectioned tissue from patient 21. Using the H&E-stained section (right), the calcification region is classified by conventional histopathological evaluation as indicated. The corresponding unstained section undergoes light optical microscopy followed by rehydration and buffer immersion for nondestructive Raman microscopy (blue shaded area) of the calcification region (black rectangle). Electron microscopy and EDS mapping (green shaded area) are performed on the region (white rectangle) after sample dehydration. Both Raman and EDS produce hyperspectral datasets, spatial maps where each *xy* point (represented by overlaid grids) has a corresponding spectrum. Datasets are represented as cubes shown spatially binned and spectrally cropped for clarity. The spatial distribution of mineral and organic matrix components is visualized by integrating over isolated peaks associated with specific signatures. Example full-resolution false color peak area heatmaps for Raman and elemental maps for EDS are shown. For the Raman dataset, averaging the apatite-containing spectra (yellow shading on the gridded image) produces the "Raman colocalized matrix spectrum," from which all organic matrix-containing compositional parameters are calculated (right). Because organic components spectrally overlap with mineral components, an additional demixed mineral spectrum is generated: the "Raman IBA spectrum," from which all Raman mineral-specific compositional parameters are calculated. Last, for the EDS map, averaging the calcium-containing pixels (green shading on the gridded image) produces the "EDS spectrum," from which all elemental ratios are calculated for the biomineralogical signature.

within nine calcification regions (6 of 101 had substantial or total whitlockite, while 3 of 101 regions had very few pixels where whitlockite was evident; see the "Whitlockite occurrences" section in Supplementary Text and figs. S5 to S8 for details). Because of uncertainty surrounding the spectrally manifested structural differences between apatite and whitlockite, whitlockite mineral metrics were not included in the analyses, although matrix-only Raman metrics (e.g., the lipid-to-protein ratio) were included. No unequivocal Raman evidence of any other phases was found, although instances of sub-Raman resolution brightly backscattering apatite-mixed nanoparticulates were encountered (figs. S9 and S10) as well as calcium phosphates below Raman resolution within necrotic regions (fig. S11).

After initial phase determination and data processing, a total of 93 individual apatite calcification regions remained and were analyzed using correlative pathology, Raman microscopy, and, where possible, EDS. Calcification pathological classification and tissue classifications were determined based on the tissue immediately surrounding the calcification (Fig. 1) within the limits of assessment using a serial section (see the "Calcification classifications" section in Supplementary Text for details). Benign calcifications were predominantly epithelial (30 of 38), i.e., located within ducts or lobules, while 4 of 38 were stromal. Within one region of duct ectasia, the calcification was situated at the interface between epithelial cells and the surrounding connective tissue (mixed). The malignant calcification population was primarily split between invasive cancer regions (26 of 50) and calcifications found within DCIS (23 of 50).

Correlative EDS mapping showed colocalization, or enrichment relative to the surrounding organic matrix, of trace elements absent from stoichiometric hydroxyapatite for all calcifications. Elements colocalized with calcium and phosphorus in >80% of calcifications included sodium, sulfur, aluminum, magnesium, chlorine, potassium, iron, and zinc. Fluorine was also detected, and although evidence of contamination from the cryotome blade prevented quantitative analysis, instances of apparent colocalization were seen as previously reported (28). Most elements appeared relatively enriched within the calcifications (for additional elemental information, see table S1).

The organic matrix colocalized with mineral, identified using Raman mapping, included general proteins (present in all calcifications), lipids (found in 68 of 93 calcifications), cell nuclei signatures (14 of 93, not counting interfacial or surrounding cells, which were numerous), heme (23 of 93 calcifications), cytochrome c–like signatures (16 of 93), carotenoids (9 of 93), and collagen (2 of 93). The surrounding organic matrices included signatures from cells, collagen, elastin, and lipids, among others. See the "Raman Data Processing" section of the Supplementary Text for Raman peak assignments (page 3) and assessment of colocalized matrix by Raman (page 4). Additionally, see the "Elemental Makeup of the Surrounding Tissue" section (page 12) of the Supplementary Text for EDS characterization of the surrounding organic matrices.

Raman microscopy captures chemical information complementary with serial pathology

Examples of calcification-containing pathologies from five patients, with corresponding local tissue and pathology classifications, H&E-stained sections (Fig. 3, A to E), von Kossa–stained sections (Fig. 3, F to J), and Raman component maps (Fig. 3, K to O), are shown in Fig. 3, where severity of pathology increases from panels (A) to (E)

(see fig. S12 for visual methods used to obtain component maps and figs. S13 and S14 for all basis maps and inverse basis spectra). Figure 3 (A, F, and K) shows a sclerosing adenosis calcification, the largest benign calcification population in this study (18 of 38 benign regions). Sclerosing adenosis is a lobular pathology involving myoepithelial proliferation, lobular fibrosis, and usually lobular epithelial atrophy (4). Calcifications frequently appear within lobules. A cluster of these calcifications can be seen in Fig. 3F. The Raman image (Fig. 3K) shows carbonated apatite calcifications interfaced by epithelial cells and associated proteins. Collagenous stroma abuts the cellular signatures.

Figure 3B centers on a duct presenting low- to intermediate-grade solid-type DCIS, in which cancer cells have proliferated within the lumen of the duct, while the ductal basement membrane and myoepithelial cell layer remain intact. Amid the cancer cells, small calcifications dot the duct interior (Fig. 3G). The Raman map (Fig. 3L) shows numerous apatite calcifications embedded within a cancer cell matrix consisting of cell nuclei signatures and cytoplasmic protein.

A case of high-grade comedo-type DCIS, defined by the region of necrosis, with cells that are poorly differentiated and likely underwent rapid and disorganized proliferation, can be seen in Fig. 3C. The von Kossa–stained section (Fig. 3H) shows a large calcification in place of the necrotic debris. Figure 3M shows that, within the mineral component, minor phase whitlockite and a substantial protein signature were found to be colocalized with apatite, the majority mineral phase. Along the mineral edge, there is evidence of cells or nuclear signatures conforming to the mineral contours. Although this could be the result of a cutting artifact, it may also suggest that cells, or cellular debris, are in active contact with mineral. Intimate cellular contact with mineral was also apparent on three-dimensional (3D) Raman analysis of an ILC calcification (figs. S15 and S16).

For nonepithelial calcifications, Fig. 3D shows a case of low-grade IDC in which invasive cancer cells have constructed duct-like structures. Calcifications are present within and around these structures (Fig. 3I). From Raman, an apatite calcification within a duct-like structure is evident (Fig. 3N), and cell nuclei, proteins, and collagen appear adjacent to the mineral.

High-grade IDC is central within Fig. 3E. In this image, the invasive cancer is flanked by adipose tissue and DCIS, and the DCIS has a band of surrounding elastin-rich stroma. Calcifications occurred within invasive cancer and DCIS (Fig. 3J). Within the invasive element, the mineral appears mixed with invasive cancer cells and stromal elements. The Raman map (Fig. 3O) depicts an intimate interface between apatite and collagen. Cellular nuclear and protein signatures border the calcification as well.

Calcifications cluster by malignancy and tissue environments based on biomineralogical signatures alone

A set of quantitative metrics derived from Raman microscopy and EDS acquired on the same calcification define a "biomineralogical signature" for each calcified region. Raman mineral metrics, calculated from an inverse basis apatite spectrum for each Raman map (Fig. 2 and fig. S12), included carbonate-to-phosphate (peak area ratio: 1070 cm^{-1}/962 cm^{-1}), which linearly correlates with weight percent carbonate in synthetic apatites (53), and the ν_1 phosphate peak full width at half maximum (FWHM), the inverse of an established measure of crystallinity/mineral maturity (47). Calcification
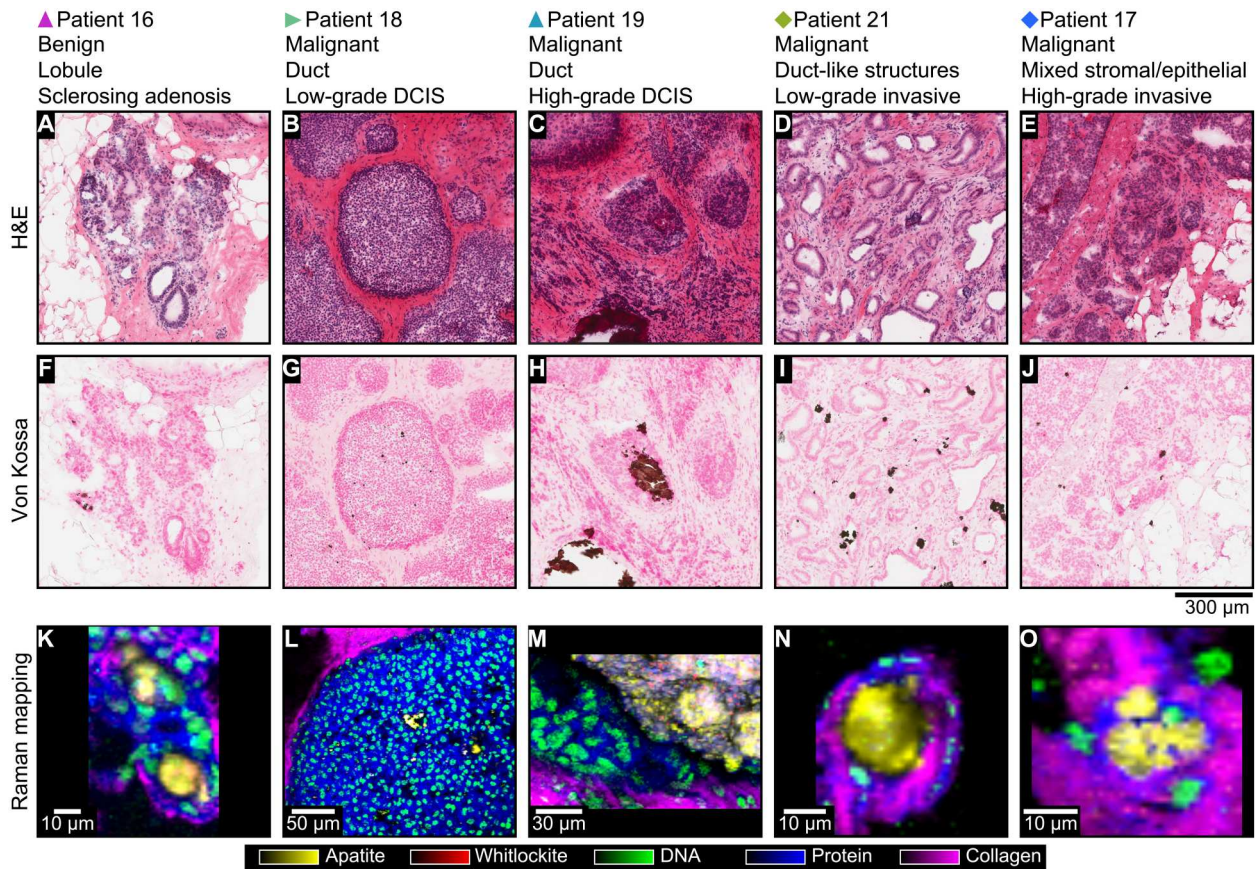
Fig. 3. Example calcification pathologies and correlated Raman mapping of calcifications. For each patient sample (columns), three serial sections were obtained: (**A** to **E**) H&E staining for pathology (cell nuclei: purple; connective and necrotic tissue: pink), (**F** to **J**) von Kossa staining for mineral identification (phosphate minerals: brown) with Nuclear Fast Red counterstaining (cell nuclei: pink), and (**K** to **O**) Raman mapping of calcifications for mineral and matrix compositional analysis, where false color heatmaps of indicated components were combined for visualization. Raman maps were taken from serially contiguous calcifications where possible [i.e., the same apparent calcification as that seen in von Kossa, as in (H) and (M)] or a nearby pathologically contiguous calcification. In addition, see Fig. 2 and figs. S12 and S13 for details of Raman processing and generation of color combination maps. Note that (M) is a maximum projection image of components from a 3D Raman scan (fig. S14), taken to capture the interface between cells and mineral. Refer to Fig. 1 for patient symbol/marker identification.

organic matrix metrics, calculated from an average spectrum of Raman map pixels containing apatite (Fig. 2), included calcification lipid-to-protein (peak area ratio: 2850 cm^{-1}/2940 cm^{-1}) and phenylalanine-to-phosphate (peak area ratio: 1006 cm^{-1}/962 cm^{-1}), chosen due to its prevalence in necrosis (28, 54). EDS analysis metrics included Ca/P, Na/Ca, Mg/Ca, Al/Ca, Fe/Ca, and Zn/Ca. Note that although Raman and EDS maps were taken from the same calcifications, they could not be perfectly aligned because of differences in spot size and focal depth between the techniques, the constraints of geometry in EDS, and the processing of both types of data.

To visualize these metrics across individual calcifications, we used hierarchical clustering. Figure 4 shows hierarchical clustering of calcification signatures (rows) from 75 calcifications from 16 patients (18 calcifications across 5 patients were excluded with missing data) using four Raman metrics and five EDS metrics. The hierarchy that emerges corresponds broadly to the local tissue environment (i.e., stroma, lobule, and duct) and immediate malignancy (i.e., the malignancy of the tissue or structures directly surrounding the calcification), among other things (see Fig. 1 and the "Calcification classifications" section of the Supplementary Text).

These data show that calcification biomineralogical signatures can differ substantially among pathologies and patients. Yet, calcification signatures across patients, sharing similar tissue and malignancy environments, had sufficient signature similarities for numerous instances of cross-patient pathology-specific cluster cohabitation.

The final (rightmost) joining reveals two stacked parent clusters with broadly disparate apatite carbonate content, phosphate v_1 FWHM, and Ca/P from EDS, all appearing to trend together. The top group (high carbonate) comprises all the stromal and most of the benign calcifications (although some mixed stromal-epithelial regions are in the lower group). The lower group (low carbonate) consists primarily of malignant ducts and low-grade duct-like invasive structures. A qualitative cluster assignment follows. Note that, for all elemental ratios excluding Ca/P, although an inverse format (e.g., 1/Na/Ca) was used for calculation of the heatmap, elemental ratios are discussed in the direction of the element-to-calcium ratio (corresponding to the direction of the color scale, which was reversed to reflect this direction as well) and are simply referred to as "Na," "Al," etc., for the following cluster assignments.

From the top group (high carbonate):

Fig. 4. Hierarchical clustering of calcifications by biomineralogical signature. Each row represents a biomineralogical signature of an individual calcification (75 total), while columns correspond to calcification compositional metrics derived from Raman microscopy and EDS mapping. Corresponding patient numbers are shown (left) and colored according to the malignancy of the tissue surrounding the given calcification. Local calcification tissue environment (Fig. 1) is indicated by an additional color column (which was not used for clustering). Parameters were standardized. Qualitative cluster assignments: cluster 1, invasive; cluster 2, reactive stroma; cluster 3, benign lobular; cluster 5, benign ductal; cluster 6, lower-grade cancer; cluster 7, large-area DCIS; cluster 8, intermediate- to high-grade DCIS. Clusters 4 and 9 are outlier clusters. A graphical legend (below the heatmap) shows, for each compositional parameter, the spectra from which the maximum (red) and minimum (blue) values (indicated) were calculated. Raman spectra are shown normalized to the apatite ν_1 phosphate peak, except for lipid/protein (normalized to the protein-rich 2940 cm^{-1} region). EDS spectra are shown normalized to the calcium K-alpha peak. Na, Al, Zn, and Mg EDS parameters are ratios, calculated, for the purposes of this heatmap, as Ca/X (rather than X/Ca used elsewhere in this study). In addition to improved data normality, this was done to maintain the conventional direction of the calcium-to-phosphorus ratio while avoiding trivial inverse correlations. For interpretability, however, the color scale for the elemental data is reversed such that red corresponds to a high X/Ca.
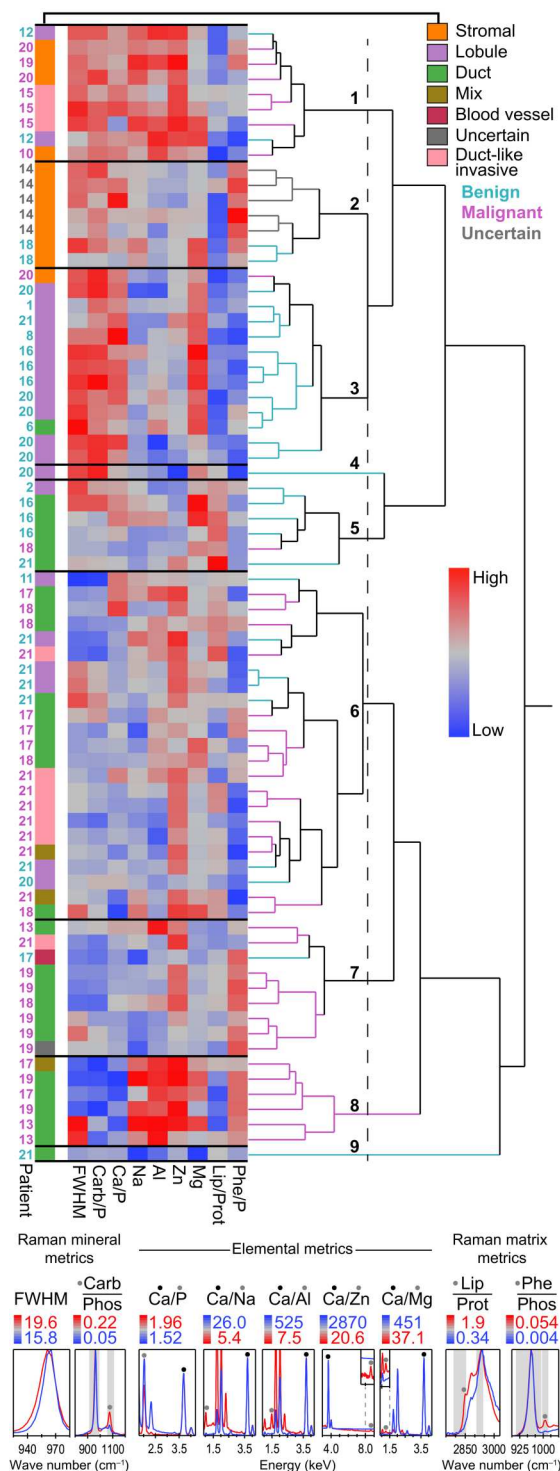
Cluster 1 (invasive) is primarily invasive stromal calcifications (three patients, two IDC and one ILC) and duct-like invasive calcifications (three from one patient). Two benign lobules (one patient) also reside in this cluster. Members of this cluster have relatively high Na, Al, and Zn.

Cluster 2 (reactive stroma) contains calcifications occurring in reactive stroma from two patients, one occurring near invasive papillary carcinoma (with uncertain immediate pathology) and one within a section containing DCIS. These calcifications appear distinct in their high phenyl-to-phosphate and have generally lower Na, Al, and Zn than cluster 1. Reactive stromal calcifications from patient 14 additionally showed evidence of colocalized cellular and cytochrome c–like signatures (data file S1) from Raman analysis,

suggesting that apoptosis may have occurred near or in association with these calcifications.

Cluster 3 (benign lobular) contains primarily benign lobular calcifications from five patients with one benign ductal and one ILC calcification. These calcifications appear to have lower phenyl-to-phosphate, Na, Al, and Zn than calcifications from clusters 1 and 2. Mg in these calcifications appears relatively high.

Cluster 4 is an isolated or outlier cluster containing a benign lobular calcification in which Zn was overall very low.

Cluster 5 (benign ductal) is composed of calcifications situated in benign (two patients) and malignant (DCIS, one patient) ducts and a calcification within a benign lobule (one patient). Cluster 5 appears distinct from other clusters within the top group with higher lipid-to-protein and overall lower carbonate-to-phosphate. Mg is relatively high here, and one calcification from patient 16 had colocalized whitlockite (fig. S6).

Within the lower group (low carbonate):

Cluster 6 (lower-grade cancer) is a mixed group containing primarily low- to intermediate-grade DCIS calcifications (two patients) and both benign and low-grade duct-like invasive calcifications from patient 21. Calcifications within duct-like invasive structures from patient 21 primarily occupy one subcluster.

Cluster 7 (large-area DCIS) is primarily composed of large-area DCIS calcifications from patient 19. All calcifications in this cluster are malignant except one (large-area) blood vessel calcification. Five of seven calcifications with colocalized carotenoid (of the 75 total calcifications within this heatmap) occur in this cluster as well (four from patient 19 and one from the blood vessel of patient 17). This cluster has the lowest Mg of all the non-outlier clusters.

Cluster 8 (intermediate- to high-grade DCIS) is exclusively malignant, consisting of intermediate- to high-grade DCIS (three patients) and one mixed stromal-epithelial region. All calcifications have high Al, Na, and Zn. Cluster 8 calcifications also have the highest relative potassium of all the clusters. Apart from patient 13, these calcifications have low carbonate-to-phosphate. Note that calcifications in patient 13 have the highest Al found within the study and that the carbonate-to-phosphate and FWHM diverge as well.

Cluster 9 is an outlier isolated cluster containing a benign duct ectasia calcification from patient 21 where Mg and Na are relatively low.

Qualitatively, these results suggest that there are numerous factors influencing calcification properties potentially including malignancy, local tissue environment, and pathology, as well as the individual patient (see the "Cluster occupancy for patients with multiple analyzed calcifications" section in Supplementary Text). Based on the variability in cluster occupancy for intrapatient calcification signatures, it would seem also that the extent of heterogeneity is variable among patients.

Carbonate content depends on multiple factors including tissue environment and malignancy

To better understand the complex relationships exhibited by the clustering, we investigated calcification metric correlations at the individual calcification level as well as metric behavior with malignancy and tissue environment at the patient level, aggregating over patients to avoid skewing results toward patients with a greater number of analyzed calcifications.

At the individual calcification level, carbonate-to-phosphate and the EDS-derived metric, Ca/P (Fig. 5A), were positively correlated ($P < 0.0001$, $R^2 = 0.30$). In addition, carbonate-to-phosphate correlated negatively with acid phosphate-to-phosphate ($P < 0.0001$, $R^2 = 0.42$; fig. S1), and carbonate-to-phosphate and FWHM were strongly positively correlated ($P < 0.0001$, $R^2 = 0.70$; fig. S1). A significant negative correlation was found between carbonate-to-phosphate and hydroxyl-to-phosphate, although there was considerable variability ($P = 0.0003$, $R^2 = 0.15$; fig. S1). (For more details, see the "Apatite mineral property trends" section in Supplementary Text.)

When aggregating by local malignancy and epithelial environment within patient samples, carbonate-to-phosphate was significantly higher and acid phosphate-to-phosphate was significantly lower in benign epithelial calcifications compared to those found in malignant epithelia ($P = 0.0093$ for carbonate-to-phosphate and $P = 0.0027$ for acid phosphate; Fig. 5, B and C), while there were no significant differences between benign and malignant calcifications located within nonepithelial tissue environments. In agreement with carbonate, Ca/P was also found to be significantly higher ($P = 0.0055$) in benign epithelial calcifications (fig. S17). These relationships were also significant without aggregation at the individual calcification level (fig. S17).

The differences in metric relationships with malignancy and potentially tissue environment prompted us to examine intratumor heterogeneity of carbonate-to-phosphate ratios within patients in which multiple calcifications were analyzed. We first examined calcifications from patient 19 where all calcifications were found in malignant pathologies, but some were in association with high-grade IDC, while others were within DCIS (Fig. 5D). A wide range of carbonate-to-phosphate ratios (0.05 to 0.16) was exhibited. Within this patient sample, the carbonate-to-phosphate was, on average, higher in calcifications found amid invasive cancer (Fig. 5E). Calcifications within DCIS with substantial surrounding fibrosis—more insulated from invasive cancer and containing calcifications that were cross-sectionally larger—had higher carbonate-to-phosphate. Figure 5F shows a Raman carbonate-to-phosphate map overlaid upon its corresponding SE image (the same calcification as in Fig. 3M). The carbonate-to-phosphate, FWHM (fig. S18), and Ca/P values (fig. S19) were lower at the edge of the calcification (closer to the cells) compared with the center. The edge of the calcification also had higher colocalized chlorine (fig. S19) compared with the center, although no correlation between carbonate-to-phosphate and chlorine was found across patients. Organic matrix gradients were also evident (fig. S18). Multiple compositional gradients and/or sharp compositional changes, including Cl and the matrix-to-phosphate ratio, were evident in another calcification region from this patient (figs. S20 and S21). Correlations between Cl content and organic matrix were conditionally evident within this patient sample but did not extend across patients (fig. S22).

Apparent intrapatient spatial trends in carbonate-to-phosphate were evident within the sample from patient 21, diagnosed with low-grade IDC, where calcifications were found associated with both benign and malignant pathologies within the same section (Fig. 5G). In this sample, calcifications within or around duct-like invasive cancer structures had, on average, lower carbonate-to-phosphate than those found associated with benign conditions. The plot in Fig. 5H shows that benign calcifications nearer to the invasive front, however, may have lower carbonate-to-phosphate
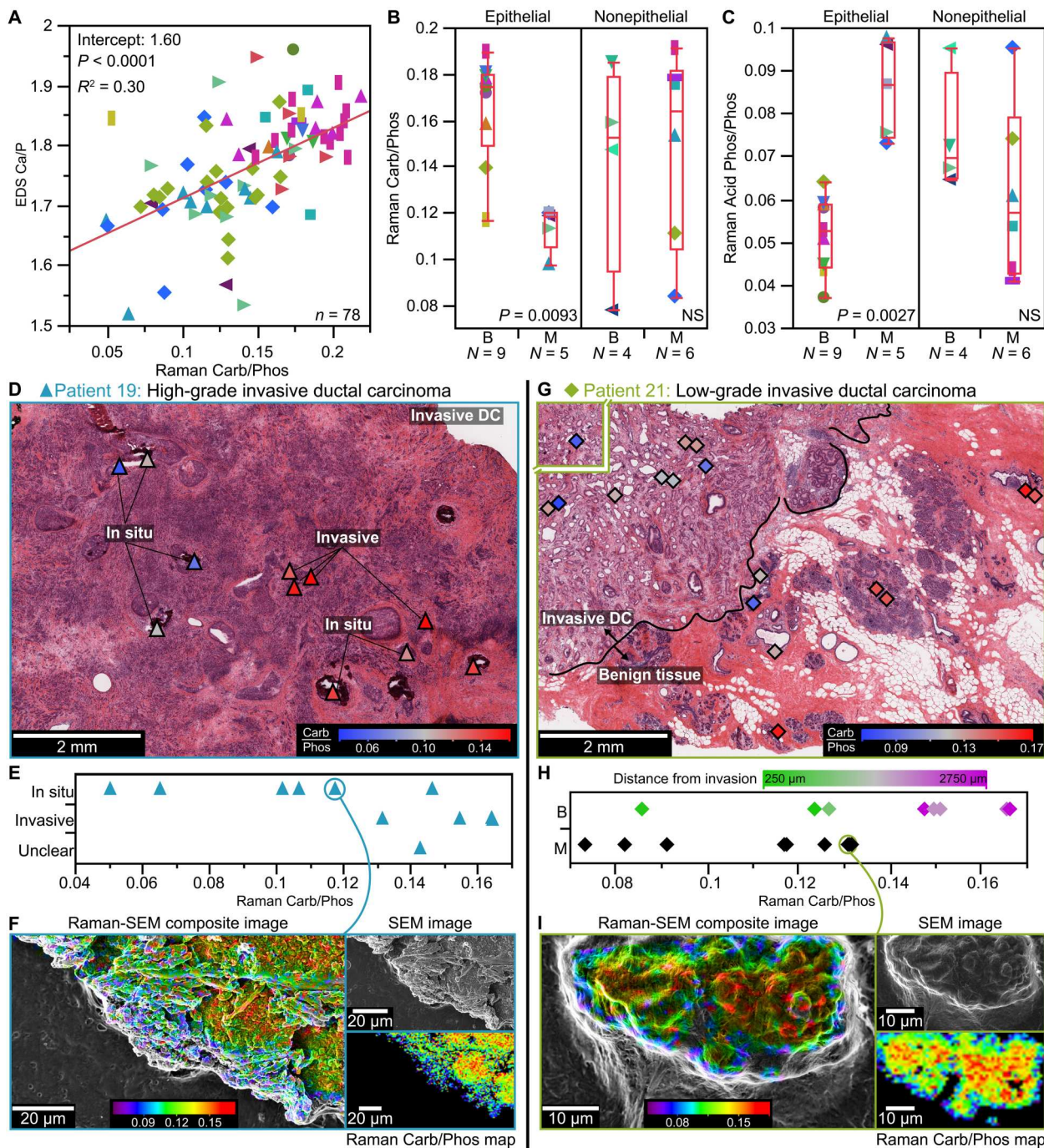
Fig. 5. Calcification carbonate content trends and heterogeneity. (**A**) EDS Ca/P correlation with Raman carbonate-to-phosphate (Carb/Phos) over individual calcifications. (**B**) Carbonate-to-phosphate and (**C**) acid phosphate-to-phosphate versus malignancy (benign, "B"; malignant, "M") by tissue type: epithelial (i.e., ductal and lobular) and nonepithelial (i.e., mixed stromal-epithelial, invasive duct-like structures, and stromal). For patients with multiple calcifications, calcification parameters carbonate-to-phosphate and Ca/P were aggregated by malignancy and tissue type (benign/epithelial, benign/nonepithelial, malignant/epithelial, malignant/nonepithelial) by taking the means. Box plots are overlaid, and *P* values were calculated using the Wilcoxon rank sum test. (**D**) H&E-stained section from patient 19 with high-grade IDC. Approximate locations of calcifications analyzed (in the serial section) are marked (triangles) and colored by the carbonate-to-phosphate ratio, with local calcification pathologies (including in situ components) indicated. (**E**) Carbonate-to-phosphate ratio versus calcification local pathology for patient 19. (**F**) From patient 19, a Raman-SEM composite image (original SE image and Raman carbonate-to-phosphate map; right), where the Raman carbonate-to-phosphate map was calculated on the basis of a stack of eight images spanning a depth of 16 μm, showing spatial distribution of carbonate within an individual calcification. (**G**) H&E-stained section from patient 21 with low-grade IDC (separated box is an invasive region outside the field of view of the primary image). Benign calcifications were also present, and the cancerous region is approximately outlined. (**H**) Carbonate-to-phosphate versus malignancy where benign calcification markers are colored by cross-sectional proximity to invasive cancer. (**I**) Raman-SEM composite image (original images; right) showing the spatial distribution of carbonate within an individual calcification in patient 21. Refer to Fig. 1 for patient marker identification.

than those farther away. Figure 5I shows a Raman-SEM (scanning electron microscopy) composite image of a calcification from the invasive region. The Raman carbonate-to-phosphate map, similar to patient 19, shows carbonate-to-phosphate lower at the edge of the calcification (see fig. S23 for average spectra). Analyses and descriptions of calcification properties from two additional patients can be found in the "Additional intrapatient and intratumor calcification property heterogeneity and trends" section in Supplementary Text and fig. S24, including one patient in which carbonate-to-phosphate in ILC calcifications was not significantly different from benign calcifications within the neighboring tissue, although elemental analysis showed clear differences based on malignancy.

Apatite colocalized zinc, iron, aluminum, and sodium are overall higher in malignant regions

Based on the hierarchical clustering (Fig. 4), in which individual clusters appeared to comprise distinctive elemental profiles, we investigated the relationship between malignancy and elemental composition of calcifications. Upon aggregating element-to-calcium values by malignancy within each patient, Zn/Ca ($P = 0.0022$), Fe/Ca ($P = 0.0073$), Al/Ca ($P = 0.017$), and Na/Ca ($P = 0.026$) (log-transformed for clarity within plots) were significantly higher in calcifications associated with malignant regions (Fig. 6). Mg/Ca trended higher in benign calcifications ($P = 0.083$), and S/Ca was significantly higher in malignant calcifications ($P = 0.048$; fig. S25). Enhanced Zn/Ca, Fe/Ca, and Al/Ca and decreased Mg/Ca in malignant versus benign were evident at the individual calcification level (fig. S26), while malignancy-based differences in Na/Ca and S/Ca were not significant.

EDS mapping data depicted in Fig. 6 (E to H) explore the enrichment of Zn, Fe, Al, and Na, showing representative malignant calcifications from the four indicated patients with corresponding calcium, phosphorus, and relevant elemental maps. Colocalization of the elements under scrutiny in Fig. 6 (A to D) with calcium and phosphorus signals is evident. Furthermore, spectra acquired within the calcium-rich regions and outside (on the neighboring organic matrix) show that these elements appear to be predominantly detected within mineral (fig. S27, where correlated histology for these calcifications can also be found), as are numerous other elements (fig. S28). These and earlier results (28) suggest that multiple elements, including those with diagnostic potential, appear enriched within the mineral. This enrichment does not preclude the possibility of elements being associated with organic matrix, particularly sodium, which was consistently detectable in the surrounding organic matrix. To probe this possibility, elements were also normalized to sulfur (see figs. S25 and S26 and the "Elemental sulfur normalization" section in Supplementary Text).

Apatite-associated lipid-to-protein ratio is reduced with patient disease severity

Both Raman apatite metrics and EDS elemental data appeared dependent on local calcification environment including malignancy, tissue environment, and local pathology. This trend was also true of matrix-to-phosphate (see the "Matrix-to-phosphate trends" section in Supplementary Text and fig. S29). To explore mineral properties in the context of breast cancer disease severity, we aggregated metrics to the patient level, averaging each calcification metric for each patient (where applicable) regardless of malignancy or tissue type. On examining Raman metrics based solely on organic

matrix colocalized with calcifications, we found a significant reduction in calcification lipid-to-protein with numerous breast cancer prognostic indicators, determined at the time of diagnosis including lymph node status ($P = 0.0079$; Fig. 7A), cancer grade ($P = 0.0053$; Fig. 7B), and cancer stage ($P = 0.0090$; Fig. 7C). Patients who later had breast cancer recurrence (all metastatic) also had lower calcification lipid-to-protein ($P = 0.052$, nonsignificant). Calcification lipid-to-protein trended nonsignificantly lower in patients taking statins ($P = 0.061$) and in calcifications from patients with estrogen receptor-negative cancers ($P = 0.056$), and there was no significant difference by HER2 status (fig. S30). Figure 7E presents a composite metric associated with the prognostic indicators in Fig. 7 (A to D), where a poor composite outcome includes patients who were lymph node positive, cancer grade III, cancer stage II or III, or had a metastatic recurrence (all estrogen receptor-negative patients also emerged within this grouping structure). Note that, even on exclusion of patients taking statins, the reduction of lipid-to-protein was still associated with overall poor composite outcome ($P = 0.0038$; fig. S30). All the aforementioned relationships at the patient level were significant at the individual calcification level, including estrogen receptor status, statin use, and metastatic cancer recurrence (fig. S31). Furthermore, substituting the protein peak area calculation with the larger-area C-H (carbon-hydrogen) stretching peak envelope in Raman maintained the same trends as lipid-to-protein, and all were also significant (fig. S32).

Figure 7 (F to H) shows calcification regions from example patients with poor and good composite outcomes: H&E, von Kossa, Raman lipid-to-protein pixel-level maps, and the averaged Raman matrix spectra (Fig. 7G, average of the apatite-containing map pixels, see Fig. 2) in order of increasing lipid-to-protein. The change in ratio is apparent as the lipid peak, normalized to protein, appears decreased in calcification examples from poor outcome patients. Note that none of the example poor outcome patient calcifications are locally malignant or occur in direct cross-sectional contact with cancer (the closest being patient 14 at 400 µm from neoplastic processes). Similarly, the calcifications from the example good outcome patients were in malignant environments as exemplified by two cases of DCIS. The third example (patient 16), found within a benign region, is the only patient in the study without a diagnosis of invasive cancer. The Raman maps display that pixel-level lipid-to-protein values are lower across calcifications overall in the poor outcome patient examples; the color shift from purple-blue to green-red is evident at the pixel level, although some intracalcification heterogeneity is present. Lipid-to-protein, however, did not appear to be sensitive to immediate tissue or malignancy environment; no significant differences were found between benign and malignant locations, epithelial versus nonepithelial locations, or benign and malignant locations grouped by epithelial and nonepithelial (fig. S33). Together, these results suggest that lipid-to-protein associated with calcifications may hold prognostic promise, potentially even in circumstances where calcifications are not overtly associated with cancer.

DISCUSSION

Using spatially correlated histopathology, Raman microscopy, and EDS, we have mapped breast calcifications within diverse chemically and histologically distinct tissue environments, providing an expanse of chemical information that complements and expands
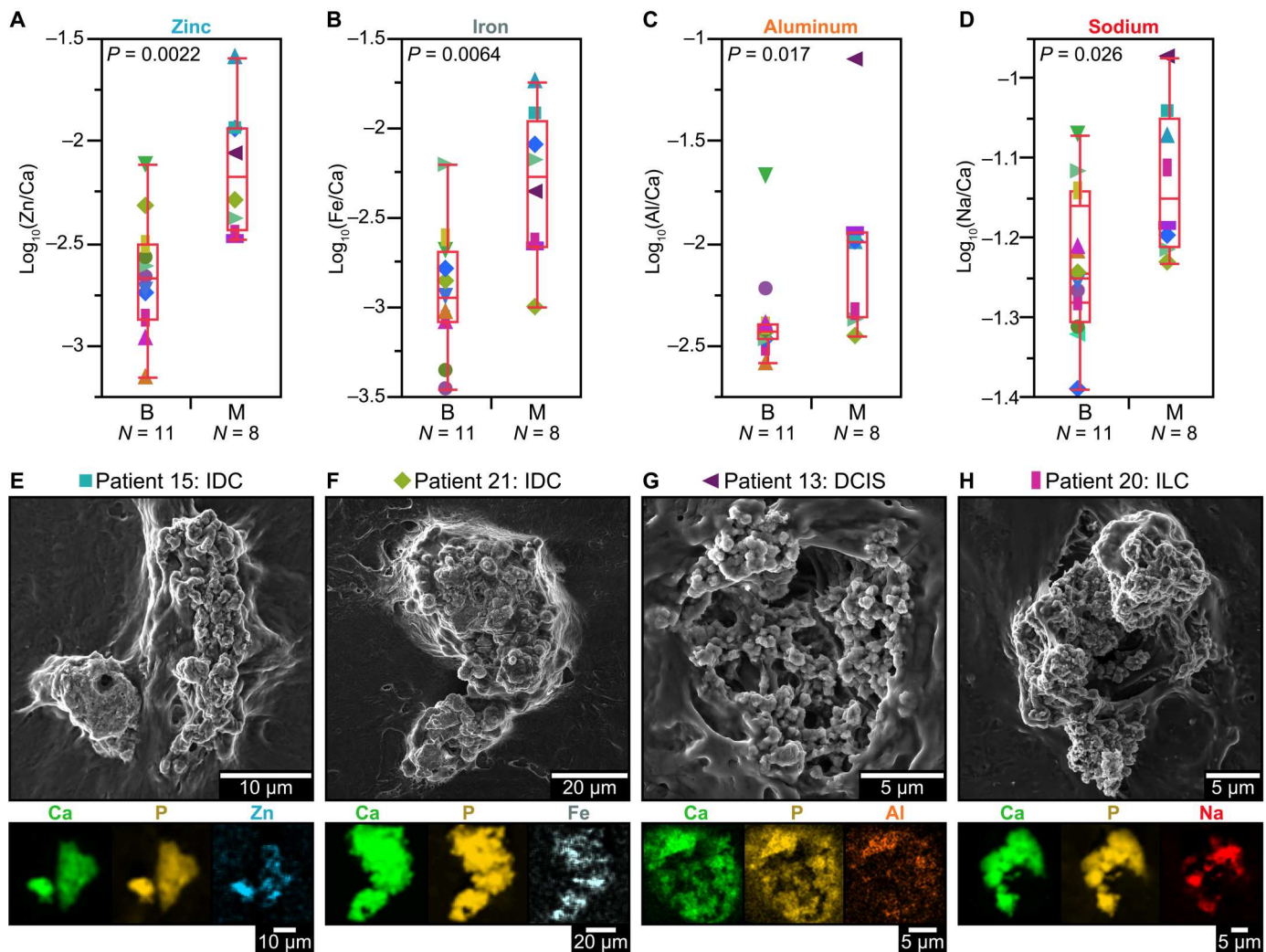
Fig. 6. Calcification trace element composition trends with local malignancy. Plots showing log-transformed (**A**) Zn/Ca, (**B**) Fe/Ca, (**C**) Al/Ca, and (**D**) Na/Ca against malignancy of calcification locale: benign or malignant. Where patients had multiple calcifications, data were aggregated into benign or malignant groups within the patient by taking the mean. Box plots are overlaid, and *P* values were calculated using the Wilcoxon rank sum test. Refer to Fig. 1 for patient symbol/marker identification. (**E** to **H**) Elemental colocalization with example calcifications from four patients (indicated). The 5-kV SE images are shown above their corresponding elemental maps for calcium, phosphorus, and the elements of interest from (A) to (D). Refer to fig. S27 for corresponding histology and EDS matrix-mineral spectral comparisons and fig. S28 for additional elemental maps.

upon traditional histopathology. Using quantitative metrics derived from Raman and EDS, we defined a biomineralogical signature and critically evaluated calcification compositional metrics in the context of pathology, tissue environment, intratumor heterogeneity, and relationships with clinical breast cancer prognostic indicators within 21 patients. We find that (i) apatite calcifications cluster into clinically meaningful and tissue environment-specific groups, based solely on their biomineralogical signature (Fig. 4). (ii) Carbonate content is sensitive to local environment, potentially reflecting tumor pH in both the trends observed and the diagnostically limiting heterogeneity (Fig. 5). (iii) Zinc, iron, aluminum, and sodium appear enhanced in malignant calcifications, in keeping with the trends of these metals observed in breast cancer tissue (Fig. 6). (iv) A calcification metric based on colocalized organic matrix composition, lipid-to-protein, was lower in patients with

poor composite outcome (Fig. 7), suggesting that pursuing organic signatures within calcifications may hold clinical value.

While malignancy and specific pathologies have been linked to microcalcification mineral properties in breast cancer (*27*, *29*, *32*), the influence of the surrounding tissue environment (e.g., epithelial versus nonepithelial and lobular versus ductal) is largely unexplored. The distinction may be an important one: In kidney deposits, for example, interstitial and intraluminal apatite calcifications can be associated with completely different pathophysiologies (*55*). We find that the biomineralogical signatures we have defined cluster not only by malignancy but also by local tissue environment. Benign lobular calcifications across numerous patients, for example, clustered together, whereas calcifications from ILC clustered with other calcifications from IDC (a cancer of different cellular lineage) that shared a similar organic matrix of collagenous
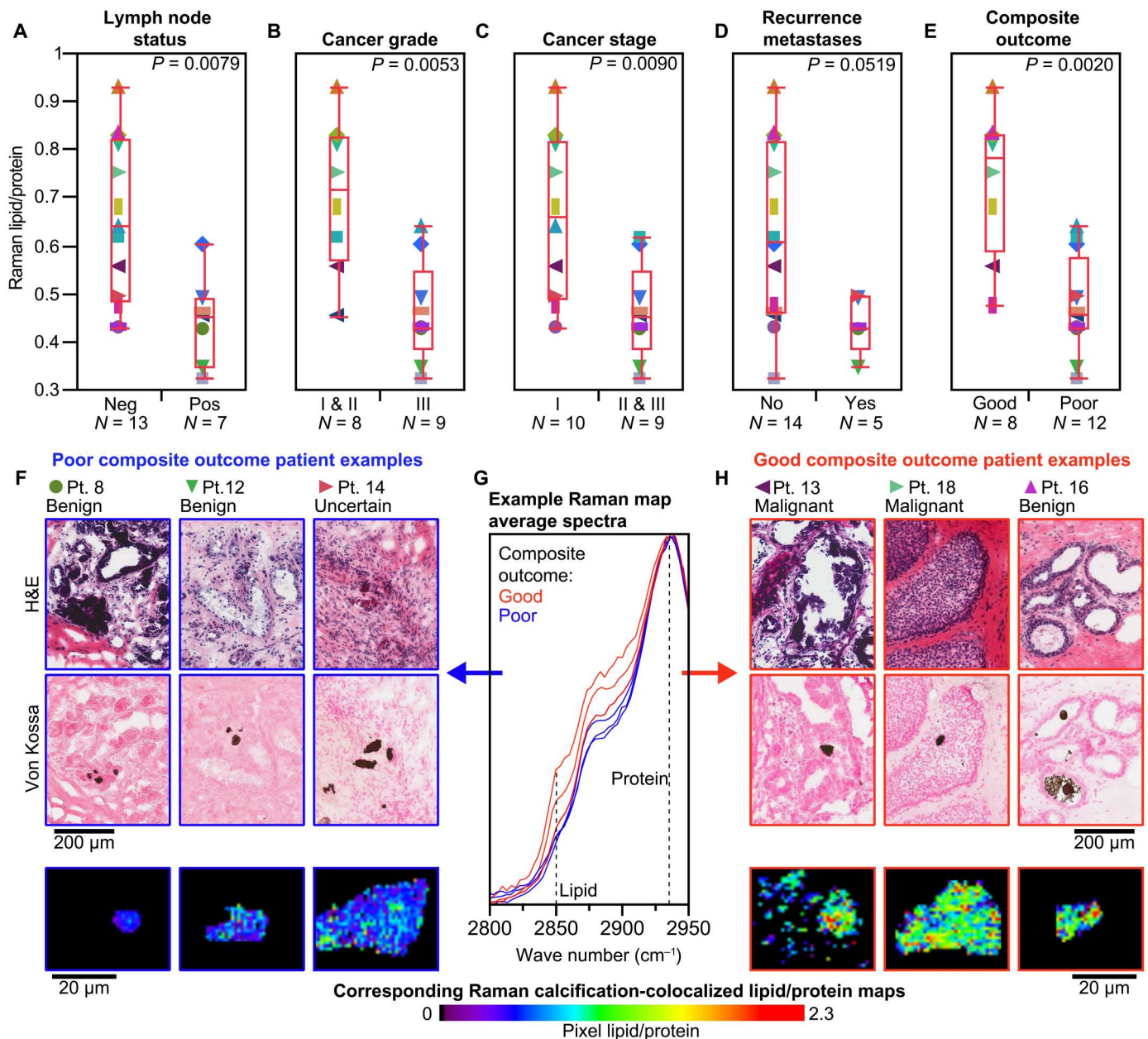
Fig. 7. Lipid-to-protein trends with cancer severity. Raman lipid-to-protein (lipid/protein) values for patients significantly differed based on clinical prognostic indicators: (**A**) lymph node status, (**B**) cancer histological grade, and (**C**) cancer stage. (**D**) Patients who later had breast cancer recurrence (all had metastases). (**E**) Combines poor outcomes from (A) to (D) to give a composite outcome. For (A) to (E), calcification data were averaged for each patient (where multiple calcifications were analyzed) regardless of tissue type or malignancy. Box plots are overlaid, and P values were calculated using the Wilcoxon rank sum test. (**F**) Example poor composite outcome patient calcification regions including local pathologies (H&E), mineral locations (von Kossa), and Raman maps of lipid/protein (shown, left to right, in order of increasing average lipid/protein values). For the Raman maps, pixels that were not colocalized with mineral were masked out (black). (**G**) Raman average spectra from the calcifications shown in the Raman lipid/protein maps from (F) and (H), normalized to the protein-rich peak at 2940 cm^{-1}, for patients with poor (blue, lower lipid-to-protein) and good (red, higher lipid-to-protein) composite outcomes. The pertinent lipid and protein peaks are indicated for clarity (although peak areas were used for the actual calculation). (**H**) Example good composite outcome patient calcification regions. Pathological classification of calcification regions for poor composite outcome patients (F): patient 8: sclerosing adenosis; patient 12: atretic lobule; patient 14: desmoplastic reactive stroma near papillary carcinoma. For good composite outcome patients (H): patient 13: low- to intermediate-grade DCIS (with freeze artifact evident); patient 18: low- to intermediate-grade DCIS; patient 16: duct ectasia. The fibroadenoma patient was excluded from lipid/protein measurements due to an artifactual skewing of the ratio by a lack of Raman-evident proteins other than collagen. Refer to Fig. 1 for patient symbol/marker identification.

stroma. This cluster comprised a contingent of high-grade nonepithelial stromal and invasive cancer calcifications that were separate from malignant ductal calcifications and, contrary to expectations (29, 32), were characterized by relatively higher carbonate-to-phosphate ratios.

Our results generally suggest that the use of calcification carbonate-to-phosphate as a prognostic or diagnostic tool, as has been proposed (27, 29, 31, 32, 56), is not straightforward. By spatially correlating the carbonate-to-phosphate ratio to local environment, we show that this ratio is sensitive to the surrounding tissue environment, proximity to cancerous tissue, and the sampling location within the calcification. While carbonate was significantly decreased in malignant versus benign epithelial calcifications, in nonepithelial environments, there was no significant difference in carbonate content between benign and malignant calcifications. In a classification scheme of high carbonate associated with benign lesions, misclassification of an invasive-adjacent benign calcification as malignant (as might be the case for patient 21) would pose no detriment to a patient with invasive cancer. Potential misclassification of invasive stromal calcifications as benign (e.g., regions from patient 19 or patient 20), however, suggests that more work is needed to understand the nature of calcification carbonate variation within tumors and if it reflects a fundamental and/or clinically accessible process of malignancy as has been previously proposed (56).

Variations in mineral properties, including carbonate content, can be influenced by a number of factors including the degree and modes of cellular involvement in mineralization (57), age or maturation of the mineral (39, 58–61), diagenesis (25), the more acidic tumor pH (56, 62, 63), and/or the alkalinity of well-established necrotic cores (64–66). Many of our observations could be consistent with the pH-based effects in and near the tumor. The extracellular pH of tumors, including breast cancer, is generally more acidic than normal tissue (62, 63), with an overall reduction in bicarbonate ions and an increase in dissolved carbon dioxide (63). There can also be considerable heterogeneity of solid tumor acidity, wrought by haphazard vascularity in tandem with varying and irregular cellular metabolic states (63), which might explain some of the variability in our findings, particularly in the nonepithelial calcification population. Overall, we found that Ca/P and carbonate-to-phosphate were correlated, and both were significantly increased in benign versus malignant epithelial calcifications, consistent with trends observed in high-pH apatites reported in synthetic studies (67, 68). In addition, we present evidence of acid phosphate enhancement in malignant epithelial calcifications, possibly indicating that malignant epithelial apatite was precipitated in an environment in which acid phosphate ions were more available (i.e., lower pH) (69). Tumor excretion of acid into the neighboring tissue (70) might also explain, by affecting forming or existing mineral, the lower carbonate of benign calcifications nearer to invasive cancer in patient 21 and/or the lower carbonate in DCIS elements that were not as insulated from invasive cancer in patient 19. A pH-based argument can also be used to explain the gradient of carbonation that has been seen here and elsewhere (31). The pH of the necrotic region that defines comedo-type DCIS is initially thought to be acidic (63, 71); however, well-established necrosis is considered alkaline (64, 65), and comedo-type ducts within human breast tumors have been reported as alkaline (66). Speculatively, a pH gradient spanning from a more alkaline necrotic core toward

acidic hypoxic viable cells could explain the carbonate gradient observed in the duct. Synthetically, higher carbonation of apatite under alkaline conditions has been observed (67), and preferential loss of carbonate has been repeatedly reported in biogenic apatites exposed to dilute acids (72).

The carbonate gradient might also be explained by mineral age/maturation; it is possible that mineral at the viable cell edge is the newest and, by uncertain mechanisms, may have lower carbonate, as observed in newly deposited bone, enamel, and dentine (59). By this logic, we can speculate that at the time of surgical extraction, the benign epithelial calcifications could simply be older than malignant epithelial calcifications, which may be consistent with mammography-based observations over time of benign versus malignant calcification growth rates (73). On the other hand, bioinformed in vitro experiments suggest that, regardless of initial carbonate content, the nature of the subsequent growth solution strongly directs the composition of the more-mature biomineral (59). Thus, mineral properties that manifest as part of the aging/maturation process are likely to be interwoven with pH, among other environmental factors.

In addition to carbonate substitution, pathological apatite deposits house a unique concentrated repository of potentially cancer-informative metal ions. We found zinc, iron, aluminum, and sodium to be concentrated within calcifications and enhanced in calcifications from malignant environments compared with benign. Apatite has an accommodating crystal lattice and is known to both incorporate ions substitutionally and/or sequester metal ions via surface interactions or intergranularly (18, 72, 74), distinctions that are not possible to make based on EDS data alone (74). Physiologically, all the elements analyzed here have been found within bone (75) and, pathologically, have been localized to calcium phosphate minerals from numerous sites within the human body (21, 76–80).

Biologically, zinc and iron homeostasis are critical to cellular function (81, 82), and their enhancement within breast cancer tissue has been frequently reported (83–89). Zinc has been found in association with numerous pathological minerals and has even been implicated in the progression of pathological mineralization (76, 77). The availability of zinc and iron to interact with mineral is likely contingent on a combination of interlinked effects: the redox state, the extent and types of systemic and/or cellular homeostatic controls, concentrations and varieties of organic and inorganic ligands, and the solution pH, among others (81, 82). In contrast, aluminum has no known biological function and in high doses is toxic. Links between chronic lower-level aluminum exposure and a number of pathologies have been proposed (90–92), and enhanced aluminum has been reported in breast cancer tissue (85, 88, 92, 93) and nipple aspirate fluid (94). The pathological association of aluminum with bioapatite has been observed, and co-enhancement with iron may be a recurring phenomenon (79, 80, 95). Last, sodium (33) has been previously reported to be significantly higher in malignant versus benign breast calcifications as well as enhanced in malignant versus normal breast tissue (84, 85).

Magnesium, an intracellular strongly hydrated divalent cation that serves as an important cofactor and complex former (96), was significantly higher in benign apatite calcifications versus malignant, though only at the individual calcification level. On hierarchical clustering of mineral metrics, the cluster containing a high occupancy of benign lobular calcifications was partly defined by

enhanced magnesium, although several studies of breast tissue have reported enhanced levels of magnesium in breast cancer versus normal tissue (83, 88, 97). Synthetic apatite and human enamel studies suggest that the uptake of magnesium into apatite is enhanced at higher carbonate concentrations and that its effectiveness as an apatite growth inhibitor is reduced at higher pH. Furthermore, like carbonate, apatite magnesium may be preferentially lost under acidic conditions (72, 98). Speculatively, this behavior may complicate interpretation of mineral magnesium content, i.e., although concentrations may be higher in cancerous conditions, the apatitic uptake may be reduced at lower pH, and high amounts of magnesium may actually inhibit apatite formation altogether (99) and/or favor the formation of another phase (e.g., whitlockite; see the "Whitlockite occurrences" in Supplementary Text and figs. S5 to S8).

Thus far, our data suggest that the local environment in which calcifications are situated may influence numerous calcification properties including carbonate content and trace element colocalization. No elemental or Raman metrics derived from the inorganic component, however, were significantly associated with patient prognostic indicators, and elemental metrics were acquired using EDS, a technique that would be challenging to integrate clinically. To assess prognostic potential, we used Raman microscopy, a clinically relevant technique, and focused on the composition of the organic matrix that was specifically associated (colocalized) with the mineral component. This approach was based on (i) the potential for calcifications to capture cancer-informative biological moieties (40) that might otherwise be mobilized or degraded (i.e., provide a "snapshot" of the organic matrix when they formed) and may even differ compositionally from the surrounding tissue (100) and (ii) the importance of the organic matrix in physiological and pathological biomineralization (14, 101). We focused on the Raman C-H stretching spectral region (2800 to 3100 cm^{-1} range), which exhibits an enhanced signal strength relative to the "fingerprint" region, and a concordant increased potential for practical clinical applications (102). By quantifying the relative contributions of two ubiquitous yet chemically distinct biological components within this spectral region, protein and lipid, we identified a key metric with prognostic potential within the calcification organic matrix: The lipid-to-protein ratio was lower in patients with poor composite outcomes.

The calcification lipid-to-protein ratio was significantly lower in the patients presenting with higher-grade cancers, higher-stage cancers, and cancers with lymph node involvement at the time of diagnosis. Three observations from the current work suggest that this ratio is rooted in mechanisms beyond the local calcification environment: First, lipid-to-protein did not show significant relationships with local malignancy or immediate tissue environment; second, low lipid-to-protein values were found for patients with diverse diagnostic presentations; last, calcification lipid-to-protein trended lower in patients taking statins versus nonstatin users. Qualitatively, low lipid-to-protein values were found within benign calcifications from poor composite outcome patients regardless of tissue environment or local pathology, potentially reflecting a metabolic shift that extends beyond the immediate environment. Calcifications from noncancerous breasts have been reported to have a lipid-rich matrix (52), and Raman breast tissue studies show enhanced lipid presence in noncancerous versus cancerous breasts (103–105), suggesting that the overall presence of

cancer could affect the lipid component of the calcification lipid-to-protein ratio. While cancer-related compositional alterations among biomolecules at the systemic level, e.g., within biofluids, are well-established phenomena (106, 107), the mechanisms by which metabolic changes—systemic, microenvironmental, or local—might influence calcification organic matrix composition remain to be understood.

Other studies, which use the same Raman bands as those used in the current study, point to a general reduction in the intensity ratio of lipid-to-protein in cervical dysplasia tissue versus normal adjacent tissue in vivo (108), cancerous brain tissue versus both negative margins tissue (109) and normal tissue in vivo (110), and colon cancer versus adjacent normal colon tissue (111). Together, these studies suggest that, although the mechanisms that drive the metric are unknown, lipid-to-protein reduction may reflect a systemic and/or cancer-informative metabolic shift that precedes or is manifest across multiple types of cancer and might extend across the diverse diagnostic presentations of the breast cancer patients exhibiting low lipid-to-protein in the current study. The ratiometric approach precludes the knowledge of which—protein, lipid, or both—drive the behavior (for futher discussion see "The lipid-to-protein ratio" section of the Supplementary Text). Regardless, if lipid-to-protein originates from a systemic mechanism, there is an enormous imperative to better understand this behavior for potential prognostic applications.

Further research is required to both validate the calcification lipid-to-protein ratio and to understand if the lipid-to-protein ratio is a metabolic reflection of a more advanced disease state and/or is truly prognostic. The exploratory design and the small number of patients ($N = 21$) in this study limit our observations to single time points (often late stage) and prohibit insights into causality. Future directions should extend our current understanding to a larger patient population including patients presenting earlier stages of disease and patients without cancer, where more benign pathologies can also be analyzed. Although lipid-to-protein remained significantly lower in poor prognosis patients after excluding statin users, we cannot deconvolute statin use from poor prognosis because four/five statin users were also patients with poor prognosis. Additional limitations include the limited number and type of benign calcifications in the current study, which were primarily situated in lobules; the variability of mineral properties among the myriad of benign "control" calcification pathologies requires further research and may provide mechanistic insights into tissue environment–based differences in mineral properties. Our analysis was biased toward calcium phosphates because of the use of the von Kossa stain for region selection, and very small calcifications were excluded. Furthermore, more sensitive mineral phase detection and/or higher resolutions could expand the biomineralogical signature and could be achieved by the complementary use of techniques such as near-edge x-ray absorption fine structure spectroscopy (112) and/or transmission electron microscopy (21). The relationships among tissue environment and calcification signatures suggest that future correlative characterization of the surrounding environment (e.g., specific cell populations, the mechanical environment, and the organic/ionic composition of ductal or lobular lumina) could be fruitful.

Regarding the organics colocalized with microcalcifications, tissue preparation methods may deplete lipids selectively, especially the use of organic solvents, and it remains to be seen if the

relationships found here are maintained using more clinically applicable tissue preparation techniques such as formalin fixation (113) and/or paraffin embedding. Using Raman, with few exceptions, we are not able to identify specific proteins and/or lipids and unraveling the metabolic mechanism(s) that may govern the lipid-to-protein ratio will require further experiments. Future work could aim to spatially resolve the specific lipid and/or protein components present in mineral by staining (e.g., Oil Red O for lipids) and/or mass spectrometry imaging (100, 114). Although the small quantity of mineral may present a challenge, omics performed on isolated calcifications could yield a potent characterization of the organics present.

The use of Raman spectroscopy, a nondestructive, label-free technique that enables the identification of characteristic chemical bond vibrations associated with numerous biological components (115), is particularly enticing for clinical applications and has seen many applications in the direction of cancer diagnosis in both ex vivo and in vivo capacities (43, 108–111, 116). Furthermore, ex vivo Raman microscopy can be both clinically compatible in terms of sample preparation and visually complementary with histopathology. Its nondestructive nature could enable a workflow of Raman analysis followed by complementary biomarker staining or targeted immunostaining, which may be crucial to exposing both biochemical and mineralogical mechanistic underpinnings amid the heterogeneous environment of breast cancer. The possibility that calcifications could preserve chemical information at their time of formation in the form of their "encapsulated" organic matrices offers the potential for both insights into pathological mineralization processes and an unused analytical axis with clinical import. Detection of calcifications has been demonstrated using spatially offset Raman through tissue as thick as 2.7 cm (117), offering the tantalizing possibility that, if calcifications do "encapsulate" valuable information, there is potential that this information could be gathered without invasive surgery.

MATERIALS AND METHODS

Experimental design

The objective of our exploratory study was to investigate the association of the biomineralogical signatures of microcalcifications in breast tissue, local pathological parameters (i.e., the tissue surrounding the calcification), and patient-level data (i.e., the overall patient diagnosis). Deidentified, banked breast carcinoma samples from the Memorial Sloan Kettering Cancer Center (MSKCC) were used in this study. These samples were collected with approval from the MSKCC Institutional Review Board. Patients were diagnosed between 2007 and 2011. Written informed consent concerning tissue specimen banking for broad research purposes was obtained from all patients before curative-intent surgery. To this end, study personnel explained the study procedure and the risks and benefits of the study to the eligible subjects. All banked specimens had been snap-frozen: Immediately after surgical removal via mastectomy, lumpectomy, or excisional biopsy, the tissue was embedded in optimal cutting temperature (OCT) compound and maintained at −80°C.

Patients with breast carcinoma (including DCIS, IDC, ILC, and Paget's disease), were selected from banked cases ($N = 40$). All patients had no evidence of distant metastasis. Radiology and pathology reports were cross-referenced and reviewed to randomly select carcinoma cases with pathology-based evidence of benign and/or malignant calcification (37 of 40) with (22 of 40) and without (18 of 40) mammographically evident calcifications. On the basis of postoperative histological evaluation, one patient was excluded because of a noncancer diagnosis of lobular carcinoma in situ. Digital preoperative mammograms were then reviewed to characterize calcifications as likely benign or suspicious. Three breast cancer samples had neither pathological nor radiological evidence of calcification, although two contained mineral when later sectioned for this study.

All samples were serially cryosectioned. For each sample, two sections underwent histological staining for local pathological assessment (H&E) and calcification identification (von Kossa) to enable systematic selection of calcification-containing sections for further analysis. All tissues in which calcifications could be identified using von Kossa, and in which they persisted through more than one section (to minimize analyzing artifactually displaced mineral), underwent Raman analysis ($N = 28$). Upon Raman analysis, seven samples were excluded on the basis of the following criteria: Mineral was below the resolution of Raman or was otherwise not detected ($N = 4$), the tissue had prohibitively delaminated in the region of interest ($N = 2$), and, in one case, the mineral was organic (not a calcification) (80). For the remaining samples ($N = 21$; see Fig. 1 for patient data and calcification pathological classification breakdown by patient), mineral properties were determined by analysis of calcifications within a final serial section using spatially correlated Raman microscopy and EDS where possible. Raman mineral properties were derived from established metrics within the physiological biomineralization community (45, 47). Raman co-localized matrix metrics (e.g., lipid-to-protein) had previously been established as an intensity ratio within the Raman cancer tissue community (108–111). Elements detected using EDS and used as mineral properties metrics are well established in both bone and pathological minerals. To maintain data quality, numerous exclusion criteria for both Raman and EDS metrics were imposed and are thoroughly described within Supplementary Text. Data file S1 includes tabulated mineral property metrics for all calcifications and patient and local pathological data.

Patient follow-up data

Breast cancer recurrence and metastasis follow-up data were acquired in July 2020. One patient stopped receiving care less than 3 months after surgery. Other than this patient and those that died of breast cancer, patient follow-up times ranged from 7.5 to 15 years (median of 12 years) including two patients who died of other or unknown causes. Breast cancer recurred in five patients with metastases in all five. Three of these metastatic patients died of breast cancer. Except for metastases, patient data were acquired at the time of diagnosis.

Tissue sectioning, histology, and histological imaging

Before sectioning, tissue blocks were transferred to a freezer at −20°C for 24 hours. Samples were sectioned on a microtome (Thermo Fisher Scientific HM550 Cryostat) at −18° to −20°C. Three serial (or as close to serial as possible) sections were cut from each sample in the following order: two 12-μm-thick sections mounted (Fisherbrand Superfrost/Plus microscope slides) for histological analysis (H&E and von Kossa/Nuclear Fast Red, respectively) and one thicker section (20 μm) mounted on a fused quartz slide

(Technical Glass Products) for correlative analyses (Raman microscopy, SE/BSE/EDS). Histological sections were air-dried and baked at 65°C for 45 min to adhere the sample to the slide and were processed at the Cornell College of Veterinary Medicine Animal Health Diagnostic Center using standard protocols for the stains. The thicker section was not baked (to preserve structure) and was stored in a desiccator for no more than a month before and during transport to Raman facilities.

All sections (histology and unstained) were imaged using a ScanScope CS0 (Aperio, Vista, CA) at ×40 magnification. Stained sections were then reviewed carefully to select regions of interest containing calcifications based on von Kossa staining (118). The histological classifications of calcification regions are described in Supplementary Text ("Calcification classifications" section).

Tissue hydration and stabilization for Raman

Tissue sections were hydrated before Raman imaging following standard hydration practices: 100, 95, 70, and 50% ethanol, followed by deionized water and then phosphate buffer, 3 to 5 min in each. Tissue delamination was an issue, possibly due to the use of fused quartz slides, particularly in benign sections that contained less stroma and more fat. To reduce the effect, the rehydration time was reduced to 3 min per solution. It is possible that mineralized matrix composition could alter with rehydration time, although, given the likely heterogeneity of density among calcifications and concordantly the variable amounts of intermixed organic matrix, it would be difficult to ascertain the effects without further experimentation. Approximate rehydration times are included in data file S1.

For Raman imaging, tissue sections were either covered by a thick bead of phosphate buffer or secured in a petri dish [using either cyanoacrylate or a stabilizing clay (Sargent Art Plastilina Modeling Clay)] and immersed in phosphate-buffered saline (PBS) (Dulbecco's PBS).

Raman microscopy setup

A confocal Raman microscope (alpha300RA, WITec, Ulm, Germany) with a frequency-doubled Nd:YAG laser (532 nm) excitation source was used (maximum power: 75 mW). The charge-coupled device detector (DU401A-BV, Andor, UK) was placed behind the spectrometer (UHTS 300, WITec, Ulm, Germany) with a grating of 600 g/mm (Blaze wavelength = 500 nm). Samples were placed on a multi-axis piezo scanner and a motorized large-area stage for sample positioning and imaged using a water immersion 60× objective [Nikon, numerical aperture (NA) = 1.0]. The lateral resolution was 0.61 λ/NA = ~325 nm. The typical mapping scanning step size used was 1 μm (though ranged from 0.5 to 2 μm) with a typical integration time of 0.23 s per step (though going as high as 4 s per step in rare cases).

Mapping data from 117 regions (from 96 individual calcifications and 5 particle-containing regions) containing Raman-detected calcifications with pathological continuity were analyzed. All Raman data were analyzed using WITec Project Plus version 4.1 and, where indicated, Igor Pro 7 (WaveMetrics Inc., Lake Oswego, OR, USA). Raman data processing is elaborated in Supplementary Text.

SEM/EDS sample preparation

Following Raman mapping, samples were dehydrated (deionized water, 50, 70, 95, and 100% ethanol, 3 to 5 min each), then air-dried, and stored in a vacuum desiccator until electron microscopy. To ready the fused quartz mounted tissue for SEM/EDS, surrounding sample-free fused quartz was scored and removed. The sample was coated with carbon to ~15 nm thick (Denton Vacuum, Desk V Sample Preparation system equipped with a carbon evaporator). Silver paint was used to improve conductivity.

Scanning electron microscopy

Coated tissue sections mounted on fused quartz were imaged using a Tescan Mira3 field-emission SEM (Czech Republic). High-resolution images of calcifications were acquired at 5 kV (working distance of 3 mm) with the in-beam SE detector and/or the in-beam backscatter detector. Using these parameters, the absorbed current was measured at 223 pA. The 5-kV SE images depicted throughout this work were autocontrasted using Fiji (119). In the cases of Fig. 6 (F and H), the Stack Focuser Fiji plugin was used (author: M. Umorin, mikeumo at sbcglobal.net) to combine two planes of focus. Raman-SEM composite image generation is described in Supplementary Text.

EDS mapping

EDS mapping was carried out at 20 kV (to ensure we did not miss higher Z elements and mitigate contribution from surface-based geometry effects) at a working distance of 15 mm using the EDS detector (XFlash Detector 6/60, Bruker, MA, USA). Under these conditions, the absorbed current was measured at 864 pA. The locations were matched to Raman mapping locations. EDS maps were acquired for at least 5 min, typically closer to 15 min. In most cases, we attempted to match the pixel diameter of the map to the spot diameter of the beam (spot size of ~5.2 μm diameter with a cross-sectional area of ~21.2 μm^2), although some regions were oversampled. Analysis was done using ESPRIT 2.1. Note that one region was excluded from all subsequent EDS data processing due to prior analysis using an alternate EDS system linked to an AirSEM, where the altered instrumental and sample conditions warranted exclusion. Thus, the total number of starting calcification regions analyzed using the described conditions was 92. EDS data processing is described in Supplementary Text. Statistical analysis and data visualization are described in Supplementary Text.

Supplementary Materials

This PDF file includes:
Supplementary Text
Figs. S1 to S35
Table S1
Legend for data file S1
References

Other Supplementary Material for this manuscript includes the following:
Data file S1

REFERENCES AND NOTES

1. L. Wilkinson, V. Thomas, N. Sharma, Microcalcification on mammography: Approaches to interpretation and biopsy. *Br. J. Radiol.* **90**, 20160594 (2017).

2. T. Tot, M. Gere, S. Hofmeyer, A. Bauer, U. Pellas, The clinical value of detecting micro-calcifications on a mammogram. *Semin. Cancer Biol.* **72**, 165–174 (2021).

3. G. M. Tse, P.-H. Tan, A. L. M. Pang, A. P. Y. Tang, H. S. Cheung, Calcification in breast lesions: Pathologists' perspective. *J. Clin. Pathol.* **61**, 145–151 (2008).

4. S. A. Hoda, E. Brogi, F. C. Koerner, P. P. Rosen, *Rosen's Breast Pathology* (Lippincott Williams & Wilkins, ed. 4, 2014).

5. A. Venkatesan, P. Chu, K. Kerlikowske, E. A. Sickles, R. Smith-Bindman, Positive predictive value of specific mammographic findings according to reader and patient variables. *Radiology* **250**, 648–657 (2009).

6. A. J. Evans, S. E. Pinder, D. R. J. Snead, A. R. M. Wilson, I. O. Ellis, C. W. Elston, The detection of ductal carcinoma in situ at mammographic screening enables the diagnosis of small, grade 3 invasive tumours. *Br. J. Cancer* **75**, 542–544 (1997).

7. G. Farshid, T. Sullivan, P. Downey, P. G. Gill, S. Pieterse, Independent predictors of breast malignancy in screen-detected microcalcifications: Biopsy results in 2545 cases. *Br. J. Cancer* **105**, 1669–1675 (2011).

8. L. Tabar, H.-H. T. Chen, M. F. A. Yen, T. Tot, T.-H. Tung, L.-S. Chen, Y.-H. Chiu, S. W. Duffy, R. A. Smith, Mammographic tumor features can predict long-term outcomes reliably in women with 1–14-mm invasive breast carcinoma: Suggestions for the reconsideration of current therapeutic practice and the TNM classification system. *Cancer* **101**, 1745–1759 (2004).

9. C. Ferranti, G. C. de Yoldi, E. Biganzoli, S. Bergonzi, L. Mariani, G. Scaperrotta, M. Marchesini, Relationships between age, mammographic features and pathological tumour characteristics in non-palpable breast cancer. *Br. J. Radiol.* **73**, 698–705 (2000).

10. S. H. Kim, E. S. Cha, C. S. Park, B. J. Kang, I. Y. Whang, A. W. Lee, B. J. Song, J. Park, Imaging features of invasive lobular carcinoma: Comparison with invasive ductal carcinoma. *Jpn. J. Radiol.* **29**, 475–482 (2011).

11. S. O'Grady, M. P. Morgan, Microcalcifications in breast cancer: From pathophysiology to diagnosis and prognosis. *Biochim. Biophys. Acta Rev. Cancer* **1869**, 310–320 (2018).

12. F. He, N. L. Springer, M. A. Whitman, S. P. Pathi, Y. Lee, S. Mohanan, S. Marcott, A. E. Chiou, B. S. Blank, N. Iyengar, P. G. Morris, M. Jochelson, C. A. Hudis, P. Shah, J. A. M. R. Kunitake, L. A. Estroff, J. Lammerding, C. Fischbach, Hydroxyapatite mineral enhances malignant potential in a tissue-engineered model of ductal carcinoma in situ (DCIS). *Biomaterials* **224**, 119489 (2019).

13. N. Vidavsky, J. A. M. R. Kunitake, A. E. Chiou, P. A. Northrup, T. J. Porri, L. Ling, C. Fischbach, L. A. Estroff, Studying biomineralization pathways in a 3D culture model of breast cancer microcalcifications. *Biomaterials* **179**, 71–82 (2018).

14. N. Vidavsky, J. A. M. R. Kunitake, L. A. Estroff, Multiple pathways for pathological calcification in the human body. *Adv. Healthc. Mater.* **10**, e2001271 (2021).

15. G. Falini, S. Albeck, S. Weiner, L. Addadi, Control of aragonite or calcite polymorphism by mollusk shell macromolecules. *Science* **271**, 67–69 (1996).

16. F. Nudelman, K. Pieterse, A. George, P. H. H. Bomans, H. Friedrich, L. J. Brylka, P. A. J. Hilbers, G. De With, N. A. J. M. Sommerdijk, The role of collagen in bone apatite formation in the presence of hydroxyapatite nucleation inhibitors. *Nat. Mater.* **9**, 1004–1009 (2010).

17. P. A. Fang, J. F. Conway, H. C. Margolis, J. P. Simmer, E. Beniash, Hierarchical self-assembly of amelogenin and the regulation of biomineralization at the nanoscale. *Proc. Natl. Acad. Sci. U.S.A.* **108**, 14097–14102 (2011).

18. L. M. Gordon, M. J. Cohen, K. W. MacRenaris, J. D. Pasteris, T. Seda, D. Joester, Amorphous intergranular phases control the properties of rodent tooth enamel. *Science* **347**, 746–750 (2015).

19. S. Amini, A. Masic, L. Bertinetti, J. S. Teguh, J. S. Herrin, X. Zhu, H. Su, A. Miserez, Textured fluorapatite bonded to calcium sulphate strengthen stomatopod raptorial appendages. *Nat. Commun.* **5**, 3187 (2014).

20. E. P. Paschalis, E. DiCarlo, F. Betts, P. Sherman, R. Mendelsohn, A. L. Boskey, FTIR microspectroscopic analysis of human osteonal bone. *Calcif. Tissue Int.* **59**, 480–487 (1996).

21. A. C. S. Tan, M. G. Pilgrim, S. Fearn, S. Bertazzo, E. Tsolaki, A. P. Morrell, M. Li, J. D. Messinger, R. Dolz-Marco, J. Lei, M. G. Nittala, S. R. Sadda, I. Lengyel, K. B. Freund, C. A. Curcio, Calcified nodules in retinal drusen are associated with disease progression in age-related macular degeneration. *Sci. Transl. Med.* **10**, eaat4544 (2018).

22. A. Y. F. You, M. S. Bergholt, J.-P. St-Pierre, W. Kit-Anan, I. J. Pence, A. H. Chester, M. H. Yacoub, S. Bertazzo, M. M. Stevens, Raman spectroscopy imaging reveals interplay between atherosclerosis and medial calcification in the human aorta. *Sci. Adv.* **3**, e1701156 (2017).

23. F. A. Shah, Micro-raman spectroscopy reveals the presence of octacalcium phosphate and whitlockite in association with bacteria-free zones within the mineralized dental biofilm. *Microsc. Microanal.* **25**, 129–134 (2019).

24. M. Daudon, C. A. Bader, P. Jungers, Urinary calculi: Review of classification methods and correlations with etiology. *Scanning Microsc.* **7**, 1081–1104 (1993).

25. M. Sivaguru, J. J. Saw, E. M. Wilson, J. C. Lieske, A. E. Krambeck, J. C. Williams, M. F. Romero, K. W. Fouke, M. W. Curtis, J. L. Kear-Scott, N. Chia, B. W. Fouke, Human kidney stones: A natural record of universal biomineralization. *Nat. Rev. Urol.* **18**, 404–432 (2021).

26. D. Bazin, I. T. Lucas, S. Rouzière, E. Elkaim, C. Mocuta, S. Réguer, D. G. Reid, J. Mathurin, A. Dazzi, A. Deniset-Besseau, M. Petay, V. Frochot, E. Letavernier, M.-C. Verpont, E. Foy, E. Bouderlique, H. Colboc, M. Daudon, Profile of an "at cutting edge" pathology laboratory for pathological human deposits: From nanometer to in vivo scale analysis on large scale facilities. *C. R. Chim.* **25**, 219–233 (2022).

27. A. Haka, K. Shafer-Peltier, M. Fitzmaurice, J. Crowe, R. R. Dasari, M. S. Feld, Identifying microcalcifications in benign and malignant breast lesions by probing differences in their chemical composition using Raman spectroscopy. *Cancer Res.* **62**, 5375–5380 (2002).

28. J. A. M. R. Kunitake, S. Choi, K. X. Nguyen, M. M. Lee, F. He, D. Sudilovsky, P. G. Morris, M. S. Jochelson, C. A. Hudis, D. A. Muller, P. Fratzl, C. Fischbach, A. Masic, L. A. Estroff, Correlative imaging reveals physiochemical heterogeneity of microcalcifications in human breast carcinomas. *J. Struct. Biol.* **202**, 25–34 (2018).

29. R. Vanna, C. Morasso, B. Marcinnò, F. Piccotti, E. Torti, D. Altamura, S. Albasini, M. Agozzino, L. Villani, L. Sorrentino, O. Bunk, F. Leporati, C. Giannini, F. Corsi, Raman spectroscopy reveals that biochemical composition of breast microcalcifications correlates with histopathologic features. *Cancer Res.* **80**, 1762–1772 (2020).

30. B. Wopenka, J. D. Pasteris, A mineralogical perspective on the apatite in bone. *Mater. Sci. Eng. C* **25**, 131–143 (2005).

31. K. S. Shin, M. Laohajaratsang, S. Men, B. Figueroa, S. M. Dintzis, D. Fu, Quantitative chemical imaging of breast calcifications in association with neoplastic processes. *Theranostics* **10**, 5865–5878 (2020).

32. R. Baker, K. D. Rogers, N. Shepherd, N. Stone, New relationships between breast microcalcifications and cancer. *Br. J. Cancer* **103**, 1034–1039 (2010).

33. R. Scott, C. Kendall, N. Stone, K. Rogers, Elemental vs. phase composition of breast calcifications. *Sci. Rep.* **7**, 136 (2017).

34. A. Romanjuk, M. Lyndin, S. Moskalenko, O. Gortinskaya, Y. Lyndina, The role of heavy metal salts in pathological biomineralization of breast cancer tissue. *Adv. Clin. Exp. Med.* **25**, 907–910 (2016).

35. Y. Zhang, C. Wang, Y. Li, A. Lu, F. Meng, F. Mei, J. Liu, K. Li, C. Yang, J. Du, Y. Li, Carbonate and cation substitutions in hydroxylapatite in breast cancer micro-calcifications. *Mineral. Mag.* **85**, 321–331 (2021).

36. A. Ben Lakhdar, M. Daudon, M.-C. Mathieu, A. Kellum, C. Balleyguier, D. Bazin, Underlining the complexity of the structural and chemical characteristics of ectopic calcifications in breast tissues through FE-SEM and μFTIR spectroscopy. *C. R. Chim.* **19**, 1610–1624 (2016).

37. F. A. Shah, Magnesium whitlockite—Omnipresent in pathological mineralisation of soft tissues but not a significant inorganic constituent of bone. *Acta Biomater.* **125**, 72–82 (2021).

38. M. Scimeca, E. Giannini, C. Antonacci, C. A. Pistolese, L. G. Spagnoli, E. Bonanno, Microcalcifications in breast cancer: An active phenomenon mediated by epithelial cells with mesenchymal characteristics. *BMC Cancer* **14**, 286 (2014).

39. R. Scott, N. Stone, C. Kendall, K. Geraki, K. Rogers, Relationships between pathology and crystal structure in breast calcifications: An in situ X-ray diffraction study in histological sections. *npj Breast Cancer* **2**, 16029 (2016).

40. M. Marro, A. M. Rodríguez-Rivero, C. Araujo-Andrade, M. T. Fernández-Figueras, L. Pérez-Roca, E. Castellà, J. Navinés, A. Mariscal, J. F. Julián, P. Turon, P. Loza-Alvarez, Unravelling the encapsulation of DNA and other biomolecules in HAp microcalcifications of human breast cancer tissues by Raman imaging. *Cancers (Basel)* **13**, 2658 (2021).

41. I. T. Lucas, D. Bazin, M. Daudon, Raman opportunities in the field of pathological calcifications. *C. R. Chim.* **25**, 83–103 (2022).

42. M. J. Baker, S. R. Hussain, L. Lovergne, V. Untereiner, C. Hughes, R. A. Lukaszewski, G. Thiéfin, G. D. Sockalingum, Developing and understanding biofluid vibrational spectroscopy: A critical review. *Chem. Soc. Rev.* **45**, 1803–1818 (2016).

43. G. W. Auner, S. K. Koya, C. Huang, B. Broadbent, M. Trexler, Z. Auner, A. Elias, K. C. Mehne, M. A. Brusatori, Applications of Raman spectroscopy in cancer diagnosis. *Cancer Metastasis Rev.* **37**, 691–717 (2018).

44. E. Tsolaki, S. Bertazzo, Pathological mineralization: The potential of mineralomics. *Materials (Basel)* **12**, 3126 (2019).

45. E. A. Taylor, E. Donnelly, Raman and Fourier transform infrared imaging for characterization of bone material properties. *Bone* **139**, 115490 (2020).

46. G. Penel, G. Leroy, C. Rey, E. Bres, MicroRaman spectral study of the PO_4 and CO_3 vibrational modes in synthetic and biological apatites. *Calcif. Tissue Int.* **63**, 475–481 (1998).

47. E. A. Taylor, C. J. Mileti, S. Ganesan, J. H. Kim, E. Donnelly, Measures of bone mineral carbonate content and mineral maturity/crystallinity for FT-IR and raman spectroscopic imaging differentially relate to physical–chemical properties of carbonate-substituted hydroxyapatite. *Calcif. Tissue Int.* **109**, 77–91 (2021).

48. M. Bennet, A. Akiva, D. Faivre, G. Malkinson, K. Yaniv, S. Abdelilah-Seyfried, P. Fratzl, A. Masic, Simultaneous raman microspectroscopy and fluorescence imaging of bone mineralization in living zebrafish larvae. *Biophys. J.* **106**, L17–L19 (2014).

49. P. Nolasco, P. V. Coelho, C. Coelho, D. F. Angelo, J. R. Dias, N. M. Alves, A. Maurício, M. F. C. Pereira, A. P. Alves De Matos, R. C. Martins, P. A. Carvalho, Mineralization of sialoliths investigated by ex vivo and in vivo x-ray computed tomography. *Microsc. Microanal.* **25**, 151–163 (2019).

50. T. Kodaka, R. Mori, K. Debari, M. Yamada, Scanning electron microscopy and electron probe microanalysis studies of human pineal concretions. *J. Electron Microsc. (Tokyo)* **43**, 307–317 (1994).

51. S. Bertazzo, E. Gentleman, K. L. Cloyd, A. H. Chester, M. H. Yacoub, M. M. Stevens, Nano-analytical electron microscopy reveals fundamental insights into human cardiovascular tissue calcification. *Nat. Mater.* **12**, 576–583 (2013).

52. O. T. Anastassiades, V. Bouropoulou, G. Kontogeorgos, M. Rachmanides, I. Gogas, Microcalcifications in benign breast diseases: A histological and histochemical study. *Pathol. Res. Pract.* **178**, 237–242 (1984).

53. A. Awonusi, M. D. Morris, M. M. J. Tecklenburg, Carbonate assignment and calibration in the Raman spectrum of apatite. *Calcif. Tissue Int.* **81**, 46–52 (2007).

54. R. A. Bitar, W. A. A. Jara, M. M. Netto, H. Martinho, L. N. Z. Ramalho, A. A. Martin, Study of human breast tissues biochemistry by FT-Raman spectroscopy. *Proc. Int. Soc. Opt. Photonics* **6093**, 60930Y (2006).

55. A. P. Evan, J. E. Lingeman, F. L. Coe, J. H. Parks, S. B. Bledsoe, Y. Shao, A. J. Sommer, R. F. Paterson, R. L. Kuo, M. Grynpas, Randall's plaque of patients with nephrolithiasis begins in basement membranes of thin loops of Henle. *J. Clin. Invest.* **111**, 607–616 (2003).

56. S. Gosling, R. Scott, C. Greenwood, P. Bouzy, J. Nallala, I. D. Lyburn, N. Stone, K. Rogers, Calcification microstructure reflects breast tissue microenvironment. *J. Mammary Gland Biol. Neoplasia* **24**, 333–342 (2019).

57. R. F. Cox, A. Hernandez-Santana, S. Ramdass, G. McMahon, J. H. Harmey, M. P. Morgan, Microcalcifications in breast cancer: Novel insights into the molecular mechanism and functional consequence of mammary mineralisation. *Br. J. Cancer* **106**, 525–537 (2012).

58. A. L. Boskey, L. Imbert, Bone quality changes associated with aging and disease: A review. *Ann. N. Y. Acad. Sci.* **1410**, 93–106 (2017).

59. M. J. Glimcher, The nature of the mineral phase in bone: Biological and clinical implications, in *Metabolic Bone Disease and Clinically Related Disorders*, L. V. Avioli, S. M. Krane, Eds. (Elsevier, ed. 3, 1998), pp. 23–50.

60. S. H. Poggi, H. C. W. Skinner, J. Ague, D. Carter, Using scanning electron microscopy to study mineral deposits in breast tissues. *Am. Mineral.* **83**, 1122–1126 (1998).

61. O. Gourgas, J. Marulanda, P. Zhang, M. Murshed, M. Cerruti, Multidisciplinary approach to understand medial arterial calcification. *Arterioscler. Thromb. Vasc. Biol.* **38**, 363–372 (2018).

62. J. L. Wike-Hooley, J. Haveman, H. S. Reinhold, The relevance of tumour pH to the treatment of malignant disease. *Radiother. Oncol.* **2**, 343–366 (1984).

63. R. J. Gillies, in *Novartis Foundation Symposium 240*, J. A. Goode, D. J. Chadwick, Eds. (Wiley, 2008), vol. 240 of *Novartis Foundation Symposia*, pp. 1–6.

64. P. W. Vaupel, S. Frinak, H. I. Bicher, Heterogeneous oxygen partial pressure and pH distribution in C3H mouse mammary adenocarcinoma. *Cancer Res.* **41**, 2008–2013 (1981).

65. P. Vaupel, F. Kallinowski, P. Okunieff, Blood flow, oxygen and nutrient supply, and metabolic microenvironment of human tumors: A review. *Cancer Res.* **49**, 6449–6465 (1989).

66. O. Hassler, Microradiographic investigations of calcifications of the female breast. *Cancer* **23**, 1103–1109 (1969).

67. D. R. Simpson, Effect of pH and solution concentration on the composition of carbonate apatite. *Am. Mineral.* **52**, 896–902 (1967).

68. I. Mayer, H. Cohen, J. C. Voegel, F. J. G. Cuisinier, Synthesis, characterization and high temperature analysis of Al-containing hydroxyapatites. *J. Cryst. Growth* **172**, 219–225 (1997).

69. N. Vandecandelaere, C. Rey, C. Drouet, Biomimetic apatite-based biomaterials: On the critical impact of synthesis and post-synthesis parameters. *J. Mater. Sci. Mater. Med.* **23**, 2593–2606 (2012).

70. V. Estrella, T. Chen, M. Lloyd, J. Wojtkowiak, H. H. Cornnell, A. Ibrahim-Hashim, K. Bailey, Y. Balagurunathan, J. M. Rothberg, B. F. Sloane, J. Johnson, R. A. Gatenby, R. J. Gillies, Acidity generated by the tumor microenvironment drives local invasion. *Cancer Res.* **73**, 1524–1535 (2013).

71. P. Swietach, S. Patiar, C. T. Supuran, A. L. Harris, R. D. Vaughan-Jones, The role of carbonic anhydrase 9 in regulating extracellular and intracellular pH in three-dimensional tumor cell growths. *J. Biol. Chem.* **284**, 20299–20310 (2009).

72. J. C. Elliott, *Structure and Chemistry of the Apatites and Other Calcium Orthophosphates* (Elsevier, 1994).

73. L. J. Grimm, M. M. Miller, S. M. Thomas, Y. Liu, J. Y. Lo, E. S. Hwang, T. Hyslop, M. D. Ryser, Growth dynamics of mammographic calcifications: Differentiating ductal carcinoma in situ from benign breast disease. *Radiology* **292**, 77–83 (2019).

74. A. Bigi, E. Boanini, M. Gazzano, Ion substitution in biological and synthetic apatites, in *Biomineralization and Biomaterials: Fundamentals and Applications* (Elsevier Inc., 2016), pp. 235–266.

75. N. B. Roberts, H. P. J. Walsh, L. Klenerman, S. A. Kelly, T. R. Helliwell, Determination of elements in human femoral bone using inductively coupled plasma atomic emission spectrometry and inductively coupled plasma mass spectrometry. *J. Anal. At. Spectrom* **11**, 133–138 (1996).

76. S. I. Djomehri, S. Candell, T. Case, A. Browning, G. W. Marshall, W. Yun, S. H. Lau, S. Webb, S. P. Ho, Mineral density volume gradients in normal and diseased human tissues. *PLOS ONE* **10**, e0121611 (2015).

77. A. Dessombz, C. Nguyen, H. K. Ea, S. Rouzière, E. Foy, D. Hannouche, S. Réguer, F. E. Picca, D. Thiaudière, F. Lioté, M. Daudon, D. Bazin, Combining μX-ray fluorescence, μXANES and μXRD to shed light on Zn²⁺ cations in cartilage and meniscus calcifications. *J. Trace Elem. Med. Biol.* **27**, 326–333 (2013).

78. G. J. Lis, J. Czapla-Masztafiak, W. M. Kwiatek, M. Gajda, E. Jasek, M. Jasinska, U. Czubek, M. Borchert, K. Appel, J. Nessler, J. Sadowski, J. A. Litwin, Distribution of selected elements in calcific human aortic valves studied by microscopy combined with SR-μXRF: Influence of lipids on progression of calcification. *Micron* **67**, 141–148 (2014).

79. D. Chappard, G. Mabilleau, D. Moukoko, N. Henric, V. Steiger, P. Le Nay, J. M. Frin, C. De Bodman, Aluminum and iron can be deposited in the calcified matrix of bone exostoses. *J. Inorg. Biochem.* **152**, 174–179 (2015).

80. J. A. M. R. Kunitake, "Correlative imaging of benign and cancerous breast calcifications: Implications for prognosis and insights into lipid dysregulation," thesis, Cornell University (2021).

81. A. Krężel, W. Maret, The biological inorganic chemistry of zinc ions. *Arch. Biochem. Biophys.* **611**, 3–19 (2016).

82. S. V. Torti, F. M. Torti, Iron and cancer: More ore to be mined. *Nat. Rev. Cancer* **13**, 342–355 (2013).

83. P. M. Santoliquido, H. W. Southwick, J. H. Olwin, Trace metal levels in cancer of the breast. *Surg. Gynecol. Obstet.* **142**, 65–70 (1976).

84. A. N. Garg, V. Singh, R. G. Weginwar, V. N. Sagdeo, An elemental correlation study in cancerous and normal breast tissue with successive clinical stages by neutron activation analysis. *Biol. Trace Elem. Res.* **46**, 185–202 (1994).

85. K.-H. Ng, D. A. Bradley, L.-M. Looi, Elevated trace element concentrations in malignant breast tissues. *Br. J. Radiol.* **70**, 375–382 (1997).

86. K. Geraki, M. J. Farquharson, D. A. Bradley, Concentrations of Fe, Cu and Zn in breast tissue: A synchrotron XRF study. *Phys. Med. Biol.* **47**, 2327–2339 (2002).

87. Y. Cui, S. Vogt, N. Olson, A. G. Glass, T. E. Rohan, Levels of zinc, selenium, calcium, and iron in benign breast tissue and risk of subsequent breast cancer. *Cancer Epidemiol. Biomarkers Prev.* **16**, 1682–1685 (2007).

88. J. Millos, M. Costas-Rodríguez, I. Lavilla, C. Bendicho, Multiple small volume microwave-assisted digestions using conventional equipment for multielemental analysis of human breast biopsies by inductively coupled plasma optical emission spectrometry. *Talanta* **77**, 1490–1496 (2009).

89. M. P. Silva, D. F. Soave, A. Ribeiro-Silva, M. E. Poletti, Trace elements as tumor biomarkers and prognostic factors in breast cancer: A study through energy dispersive x-ray fluorescence. *BMC. Res. Notes* **5**, 194 (2012).

90. C. C. Willhite, N. A. Karyakina, R. A. Yokel, N. Yenugadhati, T. M. Wisniewski, I. M. F. Arnold, F. Momoli, D. Krewski, Systematic review of potential health risks posed by pharmaceutical, occupational and consumer exposures to metallic and nanoscale aluminum, aluminum oxides, aluminum hydroxide and its soluble salts. *Crit. Rev. Toxicol.* **44**, 1–80 (2014).

91. I. O. Igbokwe, E. Igwenagu, N. A. Igbokwe, Aluminium toxicosis: A review of toxic actions and effects. *Interdiscip. Toxicol.* **12**, 45–70 (2019).

92. C. Linhart, H. Talasz, E. M. Morandi, C. Exley, H. H. Lindner, S. Taucher, D. Egle, M. Hubalek, N. Concin, H. Ulmer, Use of underarm cosmetic products in relation to risk of breast cancer: A case-control study. *EBioMedicine* **21**, 79–85 (2017).

93. H. Romanowicz-Makowska, E. Forma, M. Bryś, W. Małgorzata Krajewska, B. Smolarz, Concentration of cadmium, nickel and aluminium in female breast cancer. *Pol. J. Pathol.* **62**, 257–261 (2011).

94. F. Mannello, G. A. Tonti, V. Medda, P. Simone, P. D. Darbre, Analysis of aluminium content and iron homeostasis in nipple aspirate fluids from healthy women and breast cancer-affected patients. *J. Appl. Toxicol.* **31**, 262–269 (2011).

95. J. A. Navarro, V. A. Granadillo, O. Salgado, B. Rodríguez-Iturbe, R. García, G. Delling, R. A. Romero, Bone metal content in patients with chronic renal failure. *Clin. Chim. Acta* **211**, 133–142 (1992).

96. W. Jahnen-Dechent, M. Ketteler, Magnesium basics. *Clin. Kidney J.* **5**, i3–i14 (2012).

97. M. H. Seltzer, F. E. Rosato, M. J. Fletcher, Serum and tissue magnesium levels in human breast carcinoma. *J. Surg. Res.* **10**, 159–162 (1970).

98. R. Z. LeGeros, T. Sakae, C. Bautista, M. Retino, J. P. LeGeros, Magnesium and carbonate in enamel and synthetic apatites. *Adv. Dent. Res.* **10**, 225–231 (1996).

99. A. Babler, C. Schmitz, A. Buescher, M. Herrmann, F. Gremse, T. Gorgels, J. Floege, W. Jahnen-Dechent, Microvasculopathy and soft tissue calcification in mice are governed by fetuin-A, magnesium and pyrophosphate. *PLOS ONE* **15**, e0228938 (2020).

100. D. Taverna, F. Boraldi, G. De Santis, R. M. Caprioli, D. Quaglino, Histology-directed and imaging mass spectrometry: An emerging technology in ectopic calcification. *Bone* **74**, 83–94 (2015).

101. M. Goldberg, A. L. Boskey, *Lipids and Biomineralizations* (Gustav Fischer Verlag/VCH Publishers, 1996), vol. 31.

102. Z. Liao, M. G. Lizio, C. Corden, H. Khout, E. Rakha, I. Notingher, Feasibility of integrated high-wavenumber Raman imaging and fingerprint Raman spectroscopy for fast margin assessment in breast cancer surgery. *J. Raman Spectrosc.* **51**, 1986–1995 (2020).

103. C. J. Frank, R. L. McCreery, D. C. Redd, Raman spectroscopy of normal and diseased human breast tissues. *Anal. Chem.* **67**, 777–783 (1995).

104. A. S. Haka, K. E. Shafer-Peltier, M. Fitzmaurice, J. Crowe, R. R. Dasari, M. S. Feld, Diagnosing breast cancer by using Raman spectroscopy. *Proc. Natl. Acad. Sci. U.S.A.* **102**, 12371–12376 (2005).

105. H. Abramczyk, B. Brozek-Pluska, J. Surmacki, J. Jablonska-Gajewicz, R. Kordek, Raman "optical biopsy" of human breast cancer. *Prog. Biophys. Mol. Biol.* **108**, 74–81 (2012).

106. J. Penkert, T. Ripperger, M. Schieck, B. Schlegelberger, D. Steinemann, T. Illig, On metabolic reprogramming and tumor biology: A comprehensive survey of metabolism in breast cancer. *Oncotarget* **7**, 67626–67649 (2016).

107. L. M. Do Canto, C. Marian, R. S. Varghese, J. Ahn, P. A. Da Cunha, S. Willey, M. Sidawy, J. D. Rone, A. K. Cheema, G. Luta, M. R. N. Ranjbar, H. W. Ressom, B. R. Haddad, Metabolomic profiling of breast tumors using ductal fluid. *Int. J. Oncol.* **49**, 2245–2254 (2016).

108. J. Mo, W. Zheng, J. J. H. Low, J. Ng, A. Ilancheran, Z. Huang, High wavenumber raman spectroscopy for in vivo detection of cervical dysplasia. *Anal. Chem.* **81**, 8908–8915 (2009).

109. I. Anna, P. Bartosz, P. Lech, A. Halina, Novel strategies of Raman imaging for brain tumor research. *Oncotarget* **8**, 85290–85310 (2017).

110. J. Desroches, M. Jermyn, M. Pinto, F. Picot, M.-A. Tremblay, S. Obaid, E. Marple, K. Urmey, D. Trudel, G. Soulez, M.-C. Guiot, B. C. Wilson, K. Petrecca, F. Leblond, A new method using Raman spectroscopy for in vivo targeted brain cancer tissue biopsy. *Sci. Rep.* **8**, 1792 (2018).

111. B. Brozek-Pluska, A. Dziki, H. Abramczyk, Virtual spectral histopathology of colon cancer - biomedical applications of Raman spectroscopy and imaging. *J. Mol. Liq.* **303**, 112676 (2020).

112. O. Gourgas, K. Khan, A. Schwertani, M. Cerruti, Differences in mineral composition and morphology between men and women in aortic valve calcification. *Acta Biomater.* **106**, 342–350 (2020).

113. J. D. Moritz, S. Luftner-Nagel, J. P. Westerhof, J. W. Oestmann, E. Grabbe, Microcalcifications in breast core biopsy specimens: Disappearance at radiography after storage in formaldehyde. *Radiology* **200**, 361–363 (1996).

114. J. Lim, J. T. Aguilan, R. S. Sellers, F. Nagajyothi, L. M. Weiss, R. H. Angeletti, A. E. Bortnick, Lipid mass spectrometry imaging and proteomic analysis of severe aortic stenosis. *J. Mol. Histol.* **51**, 559–571 (2020).

115. A. C. S. Talari, Z. Movasaghi, S. Rehman, I. Rehman, Raman spectroscopy of biological tissues. *Appl. Spectrosc. Rev.* **50**, 46–111 (2015).

116. M. Sbroscia, M. Di Gioacchino, P. Ascenzi, P. Crucitti, A. di Masi, I. Giovannoni, F. Longo, D. Mariotti, A. M. Naciu, A. Palermo, C. Taffon, M. Verri, A. Sodo, A. Crescenzi, M. A. Ricci, Thyroid cancer diagnosis by Raman spectroscopy. *Sci. Rep.* **10**, 13342 (2020).

117. N. Stone, P. Matousek, Advanced transmission Raman spectroscopy: A promising tool for breast disease diagnosis. *Cancer Res.* **68**, 4424–4430 (2008).

118. D. A. Symonds, Use of the von Kossa stain in identifying occult calcifications in breast biopsies. *Am. J. Clin. Pathol.* **94**, 44–48 (1990).

119. J. Schindelin, I. Arganda-Carreras, E. Frise, V. Kaynig, M. Longair, T. Pietzsch, S. Preibisch, C. Rueden, S. Saalfeld, B. Schmid, J.-Y. Tinevez, D. J. White, V. Hartenstein, K. Eliceiri, P. Tomancak, A. Cardona, Fiji: An open-source platform for biological-image analysis. *Nat. Methods* **9**, 676–682 (2012).

120. B. L. Jolliff, J. J. Freeman, B. Wopenka, Structural comparison of lunar, terrestrial, and synthetic whitlockite using laser Raman microprobe spectroscopy. *Lunar Planet. Sci.* **27**, 613–614 (1996).

121. F. A. Shah, B. E. J. Lee, J. Tedesco, C. Larsson Wexell, C. Persson, P. Thomsen, K. Grandfield, A. Palmquist, Micrometer-sized magnesium whitlockite crystals in micropetrosis of bisphosphonate-exposed human alveolar bone. *Nano Lett.* **17**, 6210–6216 (2017).

122. G. R. Sauer, W. B. Zunic, J. R. Durig, R. E. Wuthier, Fourier transform Raman spectroscopy of synthetic and biological calcium phosphates. *Calcif. Tissue Int.* **54**, 414–420 (1994).

123. J. D. Pasteris, C. H. Yoder, B. Wopenka, Minerals in the human body: Molecular water in nominally unhydrated carbonated hydroxylapatite: The key to a better understanding of bone mineral. *Am. Mineral.* **99**, 16–27 (2014).

124. W. Peticolas, Applications of Raman spectroscopy to biological macromolecules. *Biochimie* **57**, 417–428 (1975).

125. N. K. Howell, G. Arteaga, S. Nakai, E. C. Y. Li-Chan, Raman spectral analysis in the C−H stretching region of proteins and amino acids for investigation of hydrophobic interactions. *J. Agric. Food Chem.* **47**, 924–933 (1999).

126. A. Rygula, K. Majzner, K. M. Marzec, A. Kaczor, M. Pilarczyk, M. Baranska, Raman spectroscopy of proteins: A review. *J. Raman Spectrosc.* **44**, 1061–1076 (2013).

127. B. G. Frushour, J. L. Koenig, Raman scattering of collagen, gelatin, and elastin. *Biopolymers* **14**, 379–391 (1975).

128. B. P. Gaber, W. L. Peticolas, On the quantitative interpretation of biomembrane structure by Raman spectroscopy. *Biochim. Biophys. Acta* **465**, 260–274 (1977).

129. K. Czamara, K. Majzner, M. Z. Pacia, K. Kochan, A. Kaczor, M. Baranska, Raman spectroscopy of lipids: A review. *J. Raman Spectrosc.* **46**, 4–20 (2015).

130. M. Asghari-Khiavi, A. Mechler, K. R. Bambery, D. McNaughton, B. R. Wood, A resonance Raman spectroscopic investigation into the effects of fixation and dehydration on heme environment of hemoglobin. *J. Raman Spectrosc.* **40**, 1668–1674 (2009).

131. H. G. M. Edwards, J. S. Day, Fourier transform Raman spectroscopic studies of the curing of cyanoacrylate glue. *J. Raman Spectrosc.* **35**, 555–560 (2004).

132. C. H. Yoder, J. D. Pasteris, K. N. Worcester, D. V. Schermerhorn, Structural water in carbonated hydroxylapatite and fluorapatite: Confirmation by solid state ^{2}H NMR. *Calcif. Tissue Int.* **90**, 60–67 (2012).

133. G. E. A. Mac Kinney, "Assessment of protein surface hydrophobicity by spectroscopic methods and its relation to emulsifying properties of proteins," thesis, The University of British Columbia (1994).

134. J. L. Koenig, Raman spectroscopy of biological molecules: A review. *J. Polym. Sci. Macromol. Rev.* **6**, 59–177 (1972).

135. A. C. Deymier, A. K. Nair, B. Depalle, Z. Qin, K. Arcot, C. Drouet, C. H. Yoder, M. J. Buehler, S. Thomopoulos, G. M. Genin, J. D. Pasteris, Protein-free formation of bone-like apatite: New insights into the key role of carbonation. *Biomaterials* **127**, 75–88 (2017).

136. S. Mangialardo, V. Cottignoli, E. Cavarretta, L. Salvador, P. Postorino, A. Maras, Pathological biominerals: Raman and infrared studies of bioapatite deposits in human heart valves. *Appl. Spectrosc.* **66**, 1121–1127 (2012).

137. C. Xu, R. Reed, J. P. Gorski, Y. Wang, M. P. Walker, The distribution of carbonate in enamel and its correlation with structure and mechanical properties. *J. Mater. Sci.* **47**, 8035–8043 (2012).

138. S. Cazalbou, C. Combes, D. Eichert, C. Rey, M. J. Glimcher, Poorly crystalline apatites: Evolution and maturation in vitro and in vivo. *J. Bone Miner. Metab.* **22**, 310–317 (2004).

139. K. M. Kim, Apoptosis and calcification. *Scanning Microsc.* **9**, 1137–1178 (1995).

140. V. Cottignoli, E. Cavarretta, L. Salvador, C. Valfré, A. Maras, Morphological and chemical study of pathological deposits in human aortic and mitral valve stenosis: A biomineralogical contribution. *Patholog. Res. Int.* **2015**, 342984 (2015).

141. B. O. Fowler, M. Markovic, W. E. Brown, Octacalcium phosphate. 3. Infrared and Raman vibrational spectra. *Chem. Mater.* **5**, 1417–1423 (1993).

142. B. Lafuente, R. T. Downs, H. Yang, N. Stone, *The Power of Databases: The RRUFF Project* (Walter de Gruyter GmbH, 2016).